PHYSICAL REVIEW C VOLUME 36, NUMBER 1 JULY 1987

Fission and quasifission in U-induced reactions

W. Q. Shen,* J. Albinski,† A. Gobbi, S. Gralla, K. D. Hildenbrand, N. Herrmann,
J. Kuzminski,‡ W. F. J. Müller, H. Stelzer, and J. Tōke§
Gesellschaft für Schwerionenforschung, D-6100 Darmstadt, Federal Republic of Germany

B. B. Back,** S. Bjørnholm, and S. P. Sørensen††
Niels Bohr Institute, DK-2100 Copenhagen, Denmark

(Received 24 November 1986)

Triple-differential cross sections have been measured as a function of product mass, total kinetic energy, and center-of-mass scattering angle in reactions induced by ^{238}U on ^{16}O, ^{26}Mg, ^{27}Al, ^{32}S, ^{35}Cl, ^{40}Ca, ^{48}Ca, and $^{\mathrm{nat}}$Zn targets at several bombarding energies between 4.6 and 7.5 MeV/nucleon. The analysis focuses on binary processes in which the product masses are substantially different from the target-projectile masses. These include the complete fusion followed by fission as well as quasifission processes in which large mass transfers occur on a short time scale. The relative contributions of these two components are estimated from the mass-angle correlations and analyzed within the extra and extra-extra push concepts. The time scale for mass transfer in quasifission reactions is derived from turning angles of the intermediate complex, and it is found that the mass drift toward symmetry shows the characteristics of an overdamped motion with a universal time constant independent of scattering system and bombarding energy. This is consistent with the one-body nuclear dissipation mechanism being responsible for the damping in the mass asymmetry degree of freedom. Also the average total kinetic energy of reaction products in quasifission is independent of temperature, supporting the one-body dissipation hypothesis.

I. INTRODUCTION

Nuclear reactions involving *large* mass rearrangements between the reactions partners have, until recently, been believed to fall into only two categories, namely compound nucleus fission and heavy ion fusion evaporation reactions. The characteristics of these reactions are such that the time scale for the mass transfer process is extremely difficult to establish from experimental observables. With the recently discovered process of quasifission, the situation has changed.[1–13] In this process, substantial mass rearrangements between the interacting heavy ions occur on a time scale short enough to manifest itself in the emission angle of the final products. In other words, the characteristic time for relaxation of the mass asymmetry degree of freedom during a collision is comparable with the rotational period of the intermediate complex. This gives us a unique opportunity for measuring time characteristics of the mass asymmetry relaxation mode for a wide range of systems and bombarding energies. Similar techniques have been used to gain insight into the dynamics and the time characteristics of the deep inelastic scattering process between heavy nuclei.

Conceptually, quasifission bridges the gap between the deep inelastic scattering process, where the reaction partners come in sufficiently close contact to exchange many particles, without altering their average mass, and the complete fusion process, where the reaction partners completely lose their identity by amalgamation into one compound nucleus, conserving only global properties, such as total charge, mass, and angular momentum. Quasifission reactions may be characterized by a substantial drift in mass away from the initial mass asymmetry of the interacting ions. In all cases studied so far, the drift in mass has been in the direction of symmetry, driven by the electrostatic forces which favor this behavior. In more highly asymmetric systems, the driving forces are dominated by the surface tension and go in the direction of larger asymmetry. No indications have yet been found for partial mass drift in this direction, suggesting perhaps that once motion in this direction has begun it will invariably terminate at the ultimate limit of complete fusion. Quasifission differs from the incomplete fusion process although they both have the characteristics of partial mass drift, because incomplete fusion lacks an important feature of quasifission, namely the maximum possible damping of the kinetic energy degree of freedom. The time scale and reaction mechanism behind the two processes must therefore be quite different.

In the present work we present results of a detailed experimental study of ^{238}U-induced reactions on targets of ^{16}O, ^{26}Mg, ^{27}Al, ^{32}S, ^{35}Cl, ^{40,48}Ca, and $^{\mathrm{nat}}$Zn. Some relevant properties of the systems studied are listed in Table I. By using several bombarding energies we were able to study the influence of angular momentum and temperature on the quasifission reaction. The mass drift toward symmetry was found to be almost complete for the lighter targets, e.g., ^{26}Mg and ^{27}Al; for the Ca targets a very wide range of masses spanning the entire interval between target and projectile were observed, whereas only moderate mass drifts were seen for the $^{\mathrm{nat}}$Zn target. These features have already been observed in an earlier experiment carried out at a single bombarding energy.[13] The main topic of the present work is therefore to study

TABLE I. Properties of the systems produced in the reactions with ^{238}U. The columns (1–7) give the following quantities: (1) The interaction barrier V_B in the center-of-mass system calculated by the proximity potential (Refs. 13 and 25). (2) The sum of projectile and target half-density matter radii. (3) The effective fissility parameter $(Z^2/A)_{\text{eff}}=4Z_1Z_2/[A_1^{1/3}A_2^{1/3}(A_1^{1/3}+A_2^{1/3})]$. (4) The fissility parameter Z^2/A. (5) The critical angular momentum for which the fission barrier goes to zero (Ref. 21). (6) The fission barrier for zero angular momentum which is calculated using the rotating liquid drop model (Ref. 21). (7) The mean total kinetic energy expected for symmetric fission $E_K^{\text{calc}}=0.1240Z^2/A^{1/3}$.

	Entrance channel			Composite system				
Target	V_B (MeV)	C_1+C_2 (fm)	$(Z^2/A)_{\text{eff}}$	^A_ZX	Z^2/A	$l_{B_f=0}$ ($\hbar$)	$B_f(l=0)$ (MeV)	E_K^{calc} (MeV)
^{16}O	85	9.6	21.6	$^{254}_{100}$Fm	39.4	64	1.8	196
^{26}Mg	123	10.2	26.3	$^{264}_{104}$X	41.0	56	0.86	209
^{27}Al	133	10.2	28.0	$^{265}_{105}$X	41.6	52	0.76	212
^{32}S	162	10.4	32.0	$^{270}_{108}$X	43.2	42	0.31	223
^{35}Cl	171	10.6	32.6	$^{273}_{109}$X	43.5	39	0.23	227
^{40}Ca	199	10.8	36.1	$^{278}_{112}$X	45.1	27	0.12	238
^{48}Ca	194	11.0	33.2	$^{286}_{112}$X	43.9	32	0.13	236
$^{\text{nat}}$Zn	286	11.5	43.7	$^{302}_{122}$X	49.3			275

the quasifission process as a function of bombarding energy, which affects both the temperature and the range of angular momenta of the composite systems. By including targets of Mg, S, and Cl we have further widened the scope of the study. We find that the mass asymmetry motion is dominated by a dissipative resistance which is furthermore found to be independent of temperature. This result implies that the one-body dissipation mechanism arising from the interaction of individual particles in random motion with the nuclear surface is responsible for the damping in the mass asymmetry degree of freedom.[14,15] The dissipation arising exclusively from two-body collisions between particles of short mean free path relative to the nuclear dimension would, on the contrary, give rise to viscosity terms which scale with $1/T^2$ or $1/E^*$, where E^* is the excitation energy. We have also studied the total kinetic energy of quasifission products and found results that are indistinguishable from compound nucleus fission, where the two processes can be compared. Our quasifission results extend the previous systematics considerably, both with respect to average kinetic energy and dissipation. The concept of a strong, temperature independent damping inherent in the one-body dissipation picture is again confirmed by these results.

The article is organized as follows. The experimental arrangement and the details of data acquisition and analysis are given in Sec. II, which is followed by a presentation of the experimental results in Sec. III. The measured cross sections are discussed in terms of the extra- and extra-extra-push concept in Sec. IV. The mass drift toward symmetry and the systematics of the total kinetic energy of the fragments are analyzed in Secs. V and VI, respectively, followed by a summary in Sec. VII.

II. EXPERIMENTAL ARRANGEMENT AND DATA ANALYSIS

The goal of the present experiment was to study the binary fragmentation channels for a large range of target species and uranium projectile energies in order to identify systematic features of the quasifission reaction mechanism. The cross sections for binary processes were measured over a broad range of center-of-mass angle, fragment mass, and total kinetic energy. This was achieved by using kinematic coincidence techniques in conjunction with inverse kinematics, i.e., bombarding a lighter target with a heavy projectile, in this case ^{238}U. A summary of the experimental results is presented in Table II. The kinematics of binary reactions can, in principle, be determined by measuring three appropriately chosen scalar quantities. The elimination of background arising from, e.g., target impurities and ternary processes, does, however, in practice require the determination of additional parameters. This is especially important in the present experiment where the contribution from the various target constituents of composite targets, such as ZnS and LiCl, can be separated on the basis of these additional parameters.

The experimental arrangement consists of four large area (20×30 cm^2) position sensitive avalanche detectors,[16] two of which are positioned side by side around the beam axis at a distance of ~60 cm from the target, the remaining two being situated at larger angles on opposite sides of the beam axis at a distance of ~35 cm. The detector arrangement is shown in Fig. 1. Both binary and ternary coincidences occurring in the four detectors within a resolving time of ~500–700 ps are recorded. This arrangement allows for the detection of coincident binary products over an angular range of 6°–70° in the laboratory corresponding to $\theta_{\text{c.m.}}=18°$–$162°$. The system is efficient for products spanning the entire mass range from the target to the projectile, and the complete range of fragment kinetic energies.

An identical detector arrangement and method of analysis were employed in earlier experiments as described in more detail in Ref. 13. The c.m. angular resolution and the mass resolution were $\Delta\theta_{\text{FWHM}}=2°$ (FWHM denotes full width at half maximum) and $\Delta A=5$ u, respectively.

In addition, three 7.5 cm×7.5 cm diam NaI detectors were placed at backward angles for the detection of γ rays

TABLE II. Summary of experimental results with ^{238}U beam. The columns (1–12) give the following quantities: (1) The lab energies per nucleon, $(E/A)_{\mathrm{lab}}$ (MeV/nucleon). (2) The energy in the center-of-mass system, $E_{\mathrm{c.m.}}$ (MeV). (3) The ratio of c.m. energy and interaction barrier, $E_{\mathrm{c.m.}}/V_B$. (4) The calculated grazing angular momenta $l_{\mathrm{gr}}^{\mathrm{calc}}$. (5) The calculated grazing angle in the c.m. system, $\theta_{\mathrm{gr}}^{\mathrm{calc}}$ (deg). (6) The quarter point angle, $\theta_{1/4}^{\mathrm{expt}}$(deg), extracted from measured elastic scattering angular distributions. (7) The calculated reaction cross section $\sigma_R^{\mathrm{calc}}=\pi R_{\mathrm{SA}}^2(1-V_{\mathrm{SA}}/E_{\mathrm{c.m.}})$, $V_{\mathrm{SA}}=Z_1Z_2e^2/R_{\mathrm{SA}}$. For this calculation, as well as those of the columns (4) and (5), the strong absorption radius R_{SA} was calculated in the form $R_{\mathrm{SA}}=[1.74-0.043\ln(Z_1Z_2)](A_1^{1/3}+A_2^{1/3})$. (8) The reaction cross section extracted from the measured quarter point, σ_R^{expt}(mb), $\sigma_R^{\mathrm{expt}}=\pi[(Z_1Z_2e^2/2E_{\mathrm{c.m.}})\cot(\frac{1}{2}\theta_{1/4}^{\mathrm{expt}})]^2$. (9) The cross section for the capture process σ_c^{expt}(mb), including the corrections for sequential fission. (10) The upper limit on angular momenta l_c derived from the capture cross section under the sharp cutoff assumption. (11) The mean total kinetic energy for symmetric fission, E_K^{expt} (MeV). (12) The FWHM of the total kinetic energy distribution E_K at symmetry $A/2\pm20$.

Target	$(E/A)_{\mathrm{lab}}$ (MeV)/nucleon	$E_{\mathrm{c.m.}}$ (MeV)	$E_{\mathrm{c.n.}}/V_B$	$l_{\mathrm{gr}}^{\mathrm{calc}}$ ($\hbar$)	$\theta_{\mathrm{gr}}^{\mathrm{calc}}$ (deg)	$\theta_{1/4}^{\mathrm{expt}}$ (deg)	σ_R^{calc} (mb)	σ_R^{expt} (mb)	σ_c^{expt} (mb)	l_c^{expt} ($\hbar$)	E_K^{expt} (MeV)	Γ_{E_K} (MeV)
^{16}O	5.4	81	0.96						60±5	10	191±4	48±5
	5.9	89	1.04	24	127		286		360±20	27	192±4	50±5
	6.7	101	1.19	45	91	94±2	856	760±70	730±50	41	190±4	56±5
	7.5	112	1.33	58	72	76±2	1305	1145±80	895±100	48	192±4	58±5
^{26}Mg	5.4	127	1.03	34	131	142±4	258	147±40	200±20	30	205±4	60±5
	5.9	138	1.13	59	101	108±2	699	550±60	530±50	51	204±4	63±5
	7.5	176	1.43	104	63	67±3	1713	1470±150	1390±40	93	203±4	72±5
^{27}Al	5.4	131	0.98	10	166		22		160±25	27	208±4	54±5
	5.9	143	1.08	51	114	119±2	484	395±60	330±20	42	207±4	60±5
	6.7	163	1.22	81	84	86±2	1080	1015±70	900±30	73	207±4	63±5
	7.5	182	1.37	103	68	70±3	1549	1437±50	1105±50	86	209±4	65±5
^{32}S	5.4	152	0.94						25±20	13	228±4	62±5
	6.7	189	1.17	86	93	94±2	906	860±60	610±70	70	231±4	66±5
	7.5	212	1.31	114	74	77±2	1408	1250±100	880±100	89	230±4	68±5
^{35}Cl	5.4	165	0.97						76±8	24	225±4	63±5
	5.9	180	1.05	59	120	122±2	413	378±40	290±40	49	226±4	65±5
	6.7	204	1.29	100	87	89±2	1045	988±70	720±85	82	227±4	72±5
	7.5	229	1.34	128	70	72±2	1543	1443±110	855±85	95	228±4	74±5
^{40}Ca	5.0	171	0.86						0.29±0.06	1.6		
	5.4	185	0.93						7.0±1.5	8		
	5.9	202	1.01	49	136	144±4	221	143±30	95±15	32	240±4	69±5
	6.7	229	1.15	104	95	100±3	891	738±80	470±50	73	243±4	74±5
	7.5	257	1.29	139	75	78±2	1418	1280±100	760±80	95	242±4	78±5
^{48}Ca	4.6	184	0.95						40±20	22		
	4.8	192	0.99	24	160		50		110±60	36		
	5.0	200	1.03	60	131		292		170±80	46	246±4	61±5
	5.4	216	1.11	98	104	115±4	722	482±100	410±40	73	248±4	68±5
	5.9	236	1.21	131	85	91±2	1177	959±65	710±70	98	246±4	70±5
	6.7	268	1.38	172	67	71±2	1765	1513±110	905±90	119	248±4	78±5
	7.5	360	1.54	203	55	58±2	2226	2001±160	1210±120	143	250±4	84±5
$^{\mathrm{nat}}$Zn	5.4	272	0.95						15±10	18		
	6.7	338	1.18	172	89	93±2	1126	980±70	300±50	88	272±6	98±5
	7.5	378	1.32	223	71	75±2	1689	1474±105	410±70	109	276±6	105±5

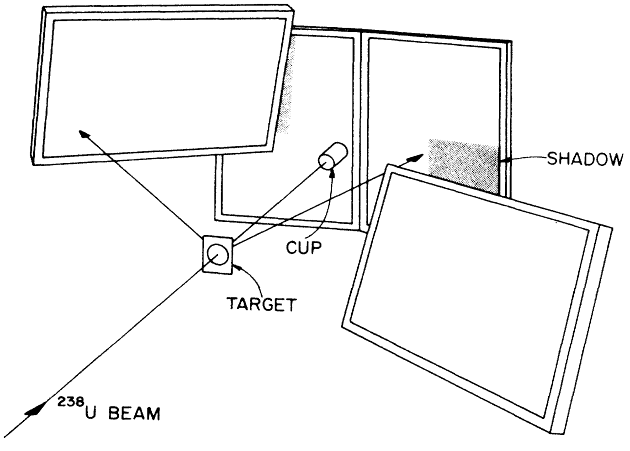

FIG. 1. Schematic illustration of the detector arrangement.

from the reaction products. The analysis and interpretation of the resulting γ-ray multiplicity data will be the subject of a separate publication. Detection and identification of single fragments were carried out simultaneously in a large position sensitive ionization chamber. The results from this detection system will also be published separately.

The Unilac accelerator delivered a pulsed ^{238}U beam with energies ranging from 4.6 to 7.5 MeV/nucleon. The time resolution of the beam was approximately 1 ns, which proved sufficient for the purpose of separating binary reaction products originating from target constituents in composite targets with widely different masses through velocity measurements.

Targets of ^{26}Mg, ^{27}Al, Li^{35}Cl, ^{40}Ca^{16}O, ^{48}Ca^{16}O, and ^{nat}Zn^{32}S of thicknesses in the range 100–300 μg/cm^2 were used. The Mg, LiCl, and ZnS targets were deposited on carbon backing foils of about 20 μg/cm^2 thickness.

The analysis of the data was carried out off line by performing a kinematical reconstruction of the binary events from the measured quantities. For each fragment, four quantities were recorded, namely the time of arrival relative to the beam pulse, the x and y positions on the detector surface, and a rough ΔE signal induced by the passage of the fragment through the detector. The velocity vector is determined on the basis of the first three quantities for each fragment. Binary reactions were selected by requiring collinear velocities of coincident products in the appropriate center-of-mass system. This requirement effectively discriminates against three body events, such as, e.g., sequential fission of the U-like reaction partner. Events in which binary products originated from reactions on the carbon backing were rejected using the same criterion. The accuracy of this type of measurement of the total mass of the scattering system is approximately $\Delta A_{\text{tot}} \sim 15$ u. For heavier targets, this is sufficient to separate reactions with the different constituents of the composite targets. In the case of the ^{26}Mg target it is, however, only marginally sufficient to separate reactions from the carbon backing and the target material. In this case a maximum contamination of $\sim 15\%$ originating from the target backing may be present in the final capture cross sections.

The high intensity of elastically scattered ^{238}U ions at the most forward angles gave rise to a significant fraction of accidental coincidences. These were effectively rejected on the basis of their large energy loss in the detectors in conjunction with flight times, which are characteristic of elastically scattered ^{238}U ions.

Having determined the velocity vectors of the legitimate binary events, the various quantities, such as the total kinetic energies, fragment masses, and center-of-mass scattering angles are calculated. The distributions with respect to these quantities are generated by weighting with the appropriate detection efficiencies, which are easily calculated for two-body processes.

The absolute normalization of the cross section was obtained from the elastic scattering at forward angles. Examples of the ratio of the measured elastic scattering cross section (which includes some inelastic and transfer reactions) to the Rutherford cross section are shown in Fig. 2 for the ^{238}U + ^{35}Cl reaction. Although the cross section measured near the grazing angle includes some contribution from inelastic and transfer reactions (due to the limited energy and mass resolution of the detection system), the constancy of this ratio at smaller angles lends credibility to the absolute cross section normalization. It should be kept in mind that the quarter point angles do not refer exclusively to elastic scattering, resulting in a systematic underestimation of the total reaction cross section from this method. This trend is evidenced by the comparison with the predicted reaction cross section, see Table II.

Finally, the triple-differential cross sections for binary events were extracted as a function of fragment mass, center-of-mass scattering angle, and total kinetic energy.

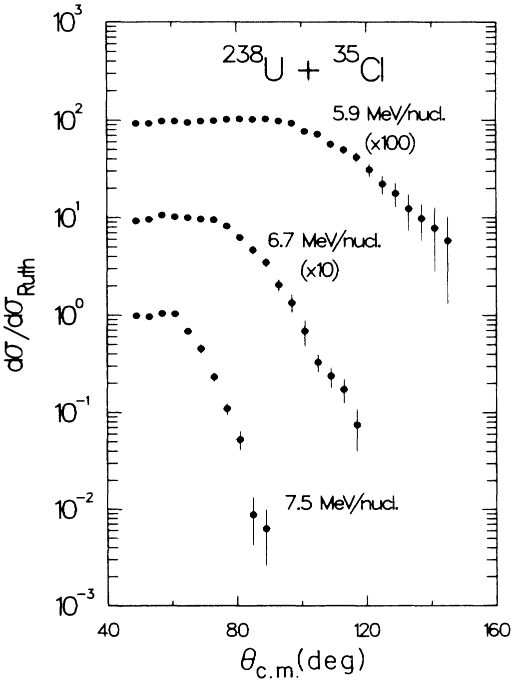

FIG. 2. Examples of the elastic scattering angular distributions. The quantity plotted is the ratio of the measured elastic scattering cross section to the Rutherford cross section for the ^{238}U + ^{35}Cl system at three energies.

The results are presented as contour diagrams of double differential cross sections, integrating over one of the variables, such as the scattering angle or the total kinetic energy.

III. EXPERIMENTAL RESULTS

The present study includes the measurements of a total of 33 complete triple-differential cross section distributions for scattering systems with a total mass ranging from 254 to 302. The amount of data demands that only a selected, but representative, subset be presented in the following subsections.

A. Mass–total kinetic energy correlations

Contour diagrams representing the angle integrated fragment mass–total kinetic energy correlations for a selected subset of the data are shown in Figs. 3 and 4. In both figures, one can distinguish two regions, a scattering region close to the target and projectile masses, and a region of capture associated with large mass transfers in the direction of symmetry; the latter component has fully relaxed energies as evidenced by the fact that the most probable total kinetic energies follow the systematics for fission fragments,[17] which are indicated by dashed curves in both figures. The almost exact independence of the total kinetic energy on the bombarding energy indicates that the initial excess kinetic energy is completely damped out and transformed into internal excitation (heat) in all capture processes. As will be discussed in more detail in Sec. VI, the reseparation of the two fragments towards scission appears to proceed as an overdamped motion where potential energy differences are largely transformed into heat. This observation leads to estimates for the dissipation constant associated with the reseparation.

B. Mass-angle correlations

The correlations between fragment mass and center of mass scattering angle integrated over the total kinetic energy distribution are shown as contour diagrams in Figs. 5 and 6 for selected reactions. Also in these diagrams, the separation between scattering and capture reactions is clearly apparent. The border line is very pronounced for the lighter targets and slowly becomes less distinct when going to the heavier targets. For the ^{238}U + ^{16}O,^{26}Mg reactions we observe symmetric mass distributions at all angles, and therefore angular distributions that are symmetric around $\theta_{\mathrm{c.m.}} = 90°$. These features are characteristic for the fission decay of a completely fused system, although they are not necessarily unique to this process. Quasifission, with a reaction time substantially longer than the characteristic time for mass drift toward symmetry and much longer than the rotational period, is also expected to show these features.[9,10] Starting with the ^{27}Al target (not shown here, see Ref. 13) a slight skewness develops, which becomes more pronounced with the ^{32}S and ^{35}Cl targets. For ^{40}Ca and heavier targets the correlation between fragment mass and scattering angle is dominated by branches leading from the target and projectile masses toward symmetry, revealing the short time scale of the process.

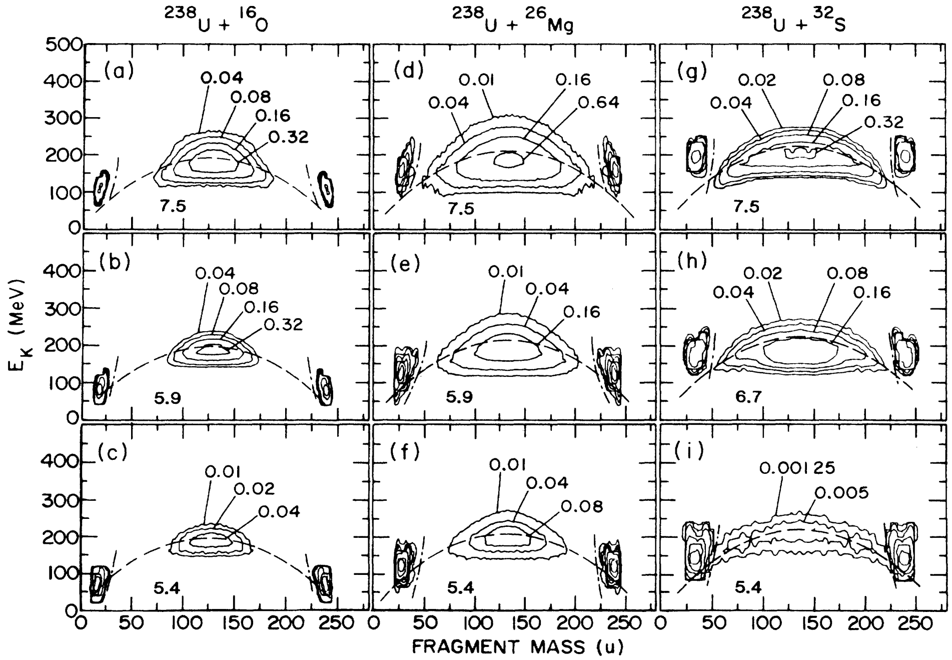

FIG. 3. Contour diagrams of the double differential cross section $d^2\sigma/(dA\,dE_k)$ (mb/nucleon MeV^{-1}) are shown as a function of the fragment mass and the total kinetic energy E_K for the reactions ^{238}U+^{16}O,^{26}Mg,^{32}S at three beam energies. The data are integrated over scattering angle.

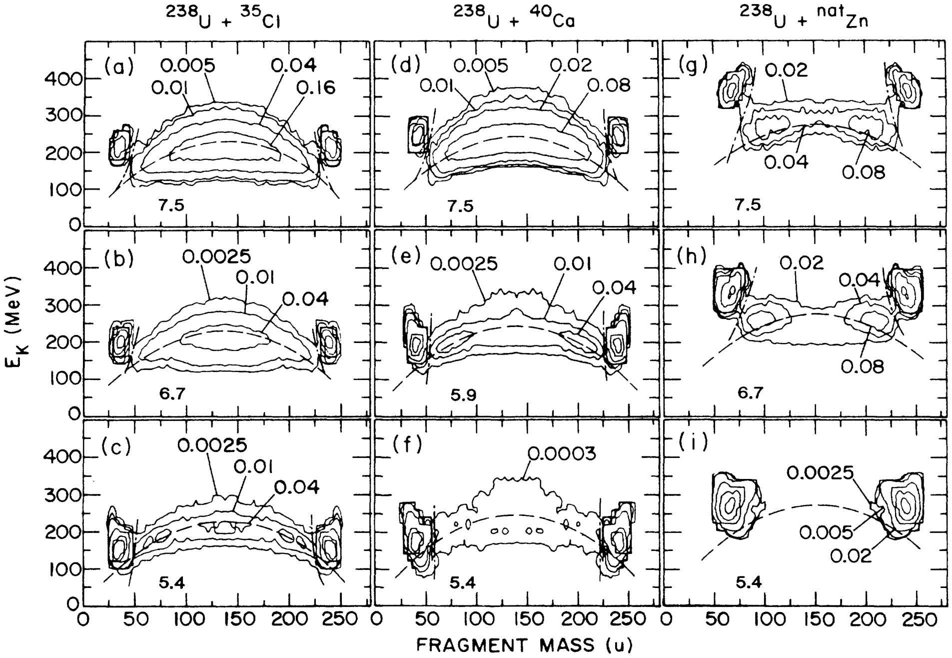

FIG. 4. Contour diagrams of the double differential cross section $d^2\sigma/(dA\,dE_k)$ (mb/nucleon MeV^{-1}) are shown as a function of the fragment mass and the total kinetic energy E_K for the reactions ^{238}U+^{35}Cl,^{40}Ca,$^{\mathrm{nat}}$Zn at three beam energies. The data are integrated over scattering angle.

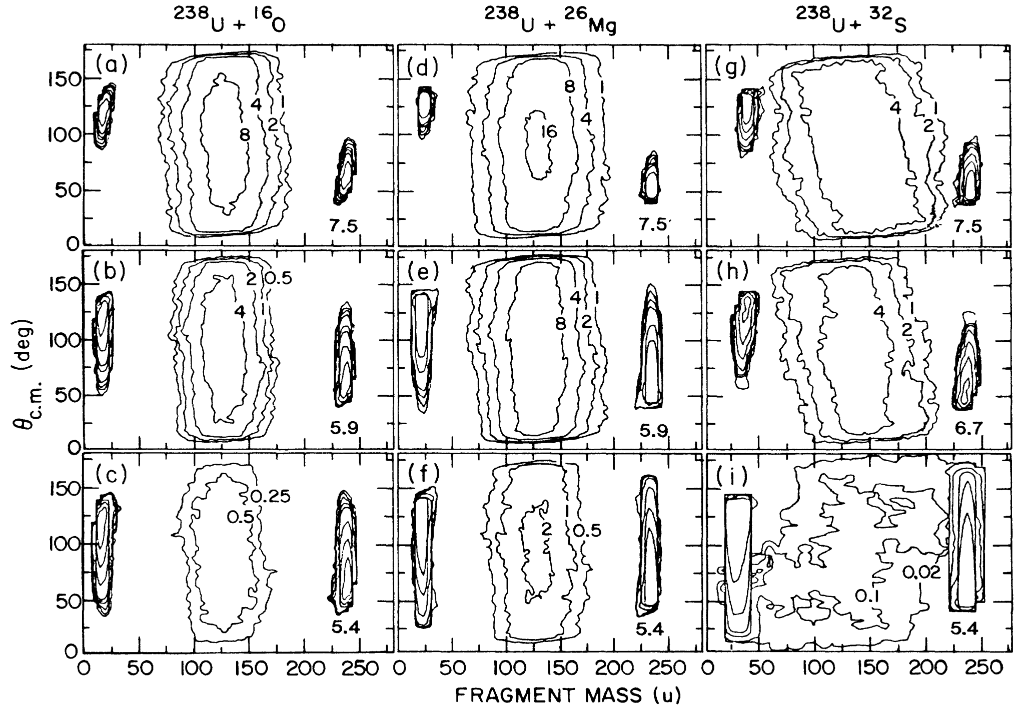

FIG. 5. Contour diagrams of the double differential cross section $d^2\sigma/(dA\,d\theta_{\mathrm{c.m.}})$ (mb/nucleon rad^{-1}) are shown as a function of the fragment mass and the center of mass angle $\theta_{\mathrm{c.m.}}$ for the reactions ^{238}U+^{16}O,^{26}Mg,^{32}S at three beam energies in each case. The data are integrated over the distribution in total kinetic energy.

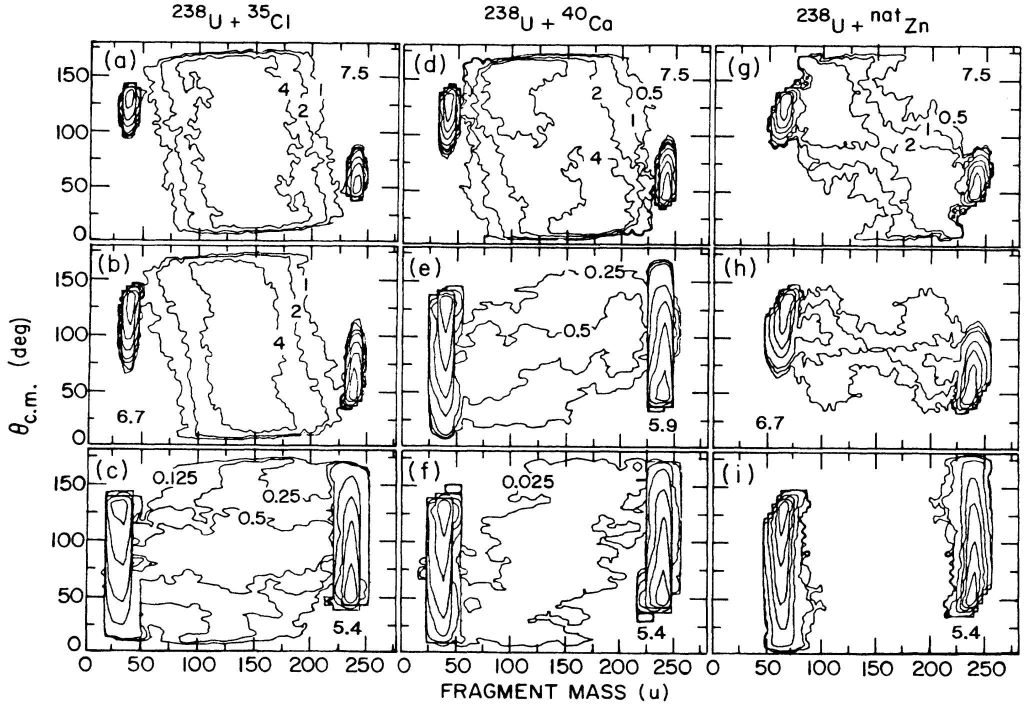

FIG. 6. Contour diagrams of the double differential cross section $d^2\sigma/(dA\, d\theta_{c.m.})$ (mb/nucleon rad^{-1}) are shown as a function of the fragment mass and the center of mass angle $\theta_{c.m.}$, for the reactions $^{238}U + ^{35}Cl, ^{40}Ca, ^{nat}Zn$ at three beam energies in each case. The data are integrated over the distribution in total kinetic energy.

C. Mass distributions

Fragment mass distributions, integrated over scattering angle and total kinetic energy, are shown in Figs. 7 and 8. The integration over center of mass scattering angle has been extended to cover the whole range by smooth extrapolations of the experimental distributions, which were measured between 18° and 162° only. When the data are examined as a function of increasing target mass (and decreasing bombarding energy) an evolution from symmetric fission-like mass distributions to a preference for mass asymmetry is clearly seen. For ^{35}Cl and heavier targets we observe a sharp decrease in the cross section for binary mass divisions into fragments heavier than $A \sim 200$ and the corresponding light fragment. This effect is attributed to the onset of sequential fission of the heavy reaction product (a three body event), processes discriminated against by the required collinearity of the velocity vectors of the fragments in the center of mass system.

Standard deviations for the mass distributions of capture, corrected for sequential fission losses and extrapolated to the whole angular range, are shown in Fig. 9 as a function of the available fragment excitation energy $E^+ = E^* + Q_0 - E_K$, see Table III. Except for a small contribution due to fragment kinetic energy and deformation energy ~ 20 MeV, it also represents the fragment excitation energy at scission. Here, E^* is the excitation energy of the would-be fused system, Q_0 is the associated ground state Q value for fission, and E_K is the total kinetic energy of the fragments equal to the Viola estimate.[17] If one makes the assumption that a statistical equilibrium with respect to the mass degree of freedom is established near the scission point, the width of the mass distribution will be a function of the mass asymmetry dependence of the potential energy surface at the scission point and the nuclear temperature. In a parabolic approximation of the potential we have

$$V(A) = \frac{k}{2}(A - A_s)^2 , \tag{1}$$

where A_s is the symmetric fragment mass and k is the restoring force constant taken to be $k = 0.0035$ MeV/u^2, in reasonable agreement with theoretical calculations.[18] In this approximation one obtains a Gaussian fragment mass distribution with a variance of

$$\sigma_A^2 = (E^+/ak^2)^{1/2} , \tag{2}$$

where a is the level density parameter taken to be $a = 30$ MeV^{-1} for nuclei in the mass range of interest. The solid curve in Fig. 9 represents this statistical equilibrium estimate of the standard deviation. With the choice of parameters made here, we obtain an estimate in good agreement with the measured mass widths for the $^{238}U + ^{16}O, ^{26}Mg$ reactions. The experimental mass widths deviate progressively from the estimate with increasing target mass, revealing the nonequilibrated character of this degree of freedom in case of heavier targets. This is already evidenced by the asymmetries of the mass-angle correlations, see Sec. III B. The rather sudden increase in the width of the fragment mass distribution was already noted in the first studies of quasifission[1–4] as an important signature for this type of reactions, but its nonequilibrium origin was not initially recognized.

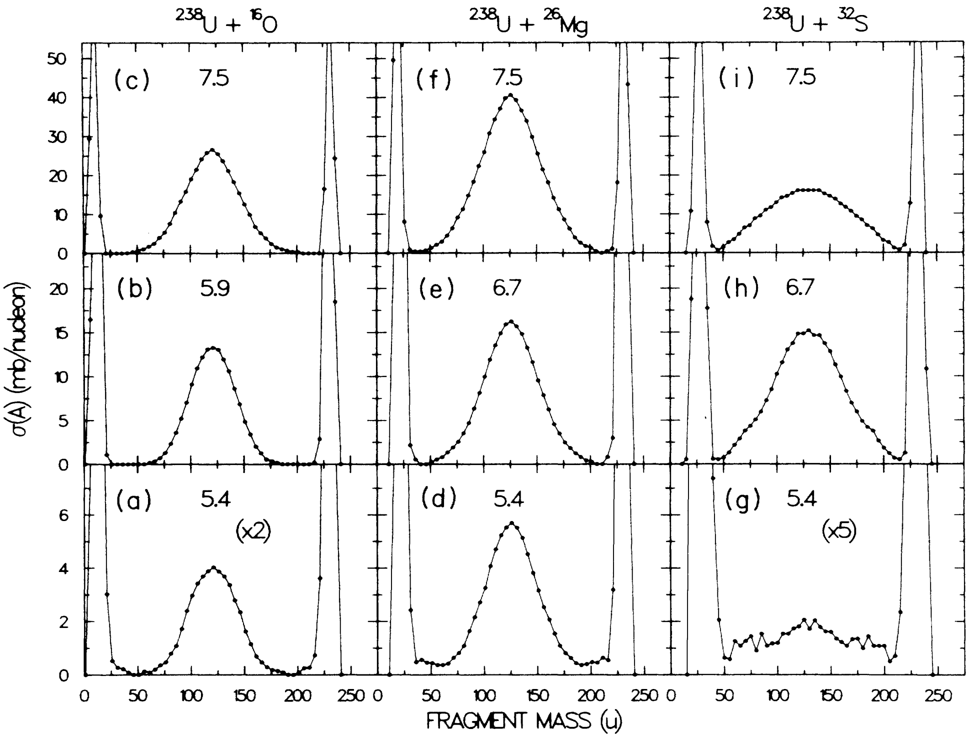

FIG. 7. Distributions of fragment masses, integrated over total kinetic energy and center of mass scattering angle, are shown for the reactions $^{238}U + ^{16}O, ^{26}Mg, ^{32}S$ at three beam energies.

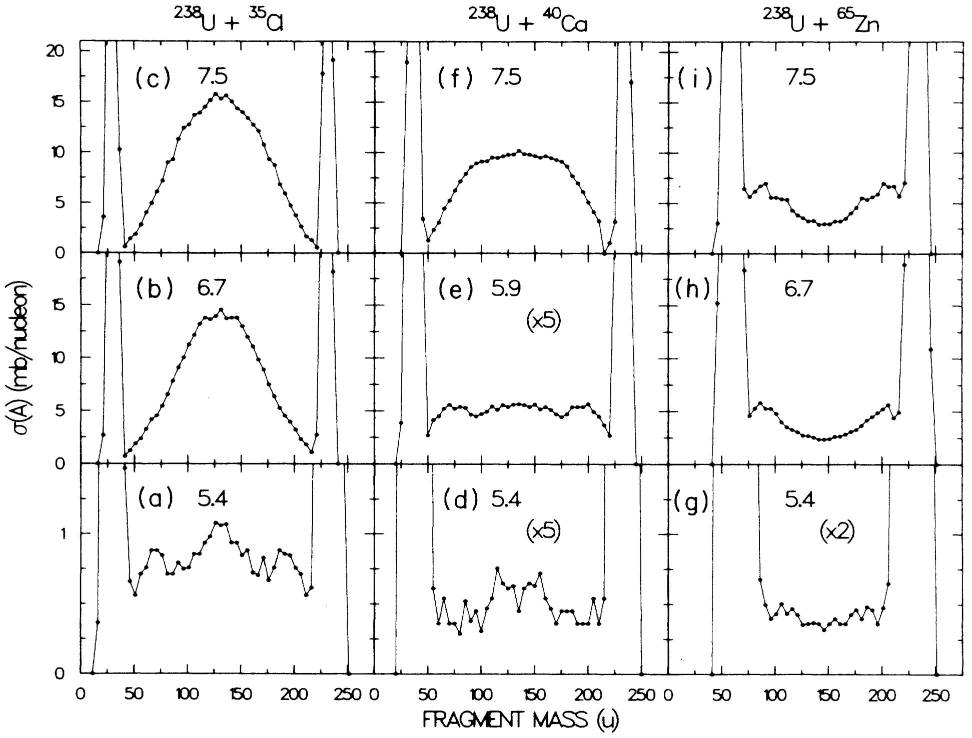

FIG. 8. Distributions of fragment masses, integrated over total kinetic energy and center of mass scattering angle, are shown for the reactions $^{238}U + ^{35}Cl, ^{40}Ca, ^{nat}Zn$ at three beam energies.

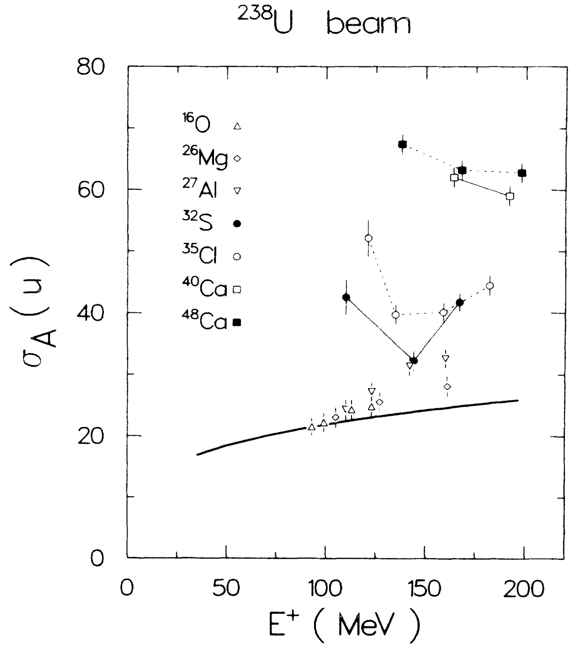

FIG. 9. The standard deviation of the mass distribution of fission-like products is shown as a function of the excitation energy at the scission point, E^+. The thick solid curve is calculated on the basis of Eq. (2).

D. Angular distributions

Examples of the angular distributions for capture events are shown in panels (a) and (b) in Fig. 10 for the ^{238}U$+^{16}$O,^{27}Al reactions. The solid curves represent the best fit to the data on the basis of the standard theoretical expression. This applies to the fission decay of compound of nuclei with sufficient excitation energy to justify a statistical treatment. In this case the angular distribution is given by[10]

$$W(\theta)=\sum_{I=0}^{\infty}(2I+1)T_I\sum_{K=-I}^{I}\rho_I(K)\,|\mathcal{D}^I_{0K}(\theta)|^2\,, \tag{3}$$

where the $\mathcal{D}$ function is summed over the distributions of spin, I, and its projection, K, onto the nuclear symmetry axis. The spin distribution $(2I+1)T_I$ is computed by incorporating the smoothing effects of interaction barrier fluctuations arising from both static target deformations and surface vibrations.[10] Using rather general arguments,[10,19,20] the appropriate K distributions are expected to be of Gaussian form,

$$\rho(K)\propto\exp(-K^2/2K_0^2)\,. \tag{4}$$

The experimental angular distributions shown in Fig. 10 are reproduced by adjusting the variance K_0^2 of the K distribution, the results of which are shown in Fig. 11 as solid points and listed in Table IV.

Recently, much attention has been devoted to the question of where along the path to fission the K distribution is determined. The standard theory is based on the assumption that this occurs at the fission saddle point by ar-

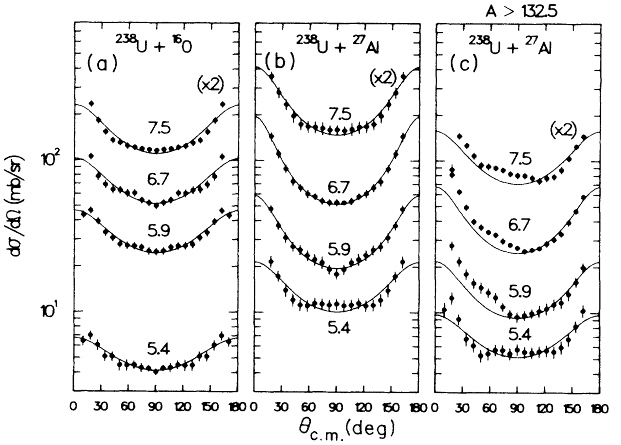

FIG. 10. Angular distribution of fission-like products are shown as solid points for the ^{238}U$+^{16}$O and ^{238}U$+^{27}$Al reactions in panels (a) and (b), respectively. Solid curves represent best fits to the data using Eq. (3). In panel (c) the angular distribution of fission-like products with masses $A>132.5$ u are shown. The solid curves represent the best fits to the backward part, $\theta>90°$, of the angular distributions.

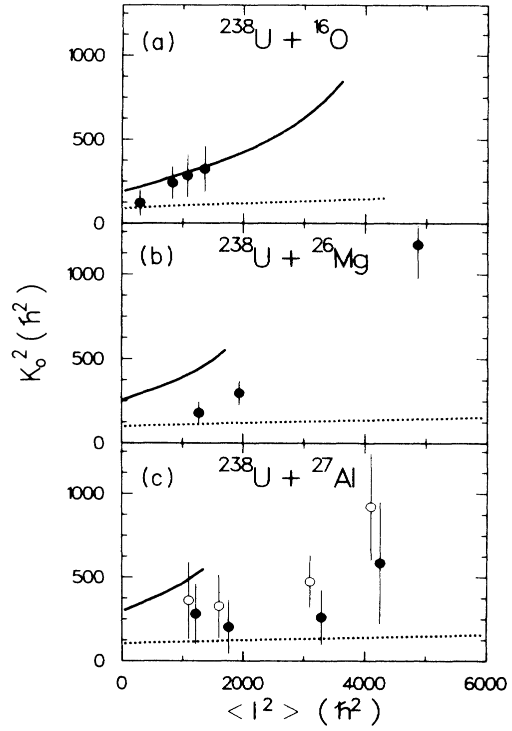

FIG. 11. The variances of the K distributions are shown (solid points) as a function of the mean square spin of the fissioning system for the reactions ^{238}U$+^{16}$O, ^{238}U$+^{26}$Mg, and ^{238}U$+^{27}$Al in panels (a), (b), and (c), respectively. The solid curves represent the predictions of the saddle point model based on the saddle shapes given by the rotating liquid drop model whereas the dashed curves are calculated on the basis of the rigid scission point model (Ref. 9). Open circles for the ^{238}U$+^{27}$Al reaction are obtained from the fits of the backward scattered fragments of mass $A>132.5$ u.

TABLE III. Excitation energy of composite systems.

Target	$(E/A)_{\text{lab}}$ (MeV)/nucleon	Q_{gg} (MeV)	E^* (MeV)	Q_0 (MeV)	$E^{+\text{a}}$ (MeV)	σ_A^{expt} (u)
^{16}O	5.4	39.6	42	242	93	21.5±1.5
	5.9		49		99	22.2±1.6
	6.7		61		113	24.3±1.6
	7.5		73		123	24.8±1.7
^{26}Mg	5.4	79.5	47	268	110	23.0±1.7
	5.9		59		123	25.5±1.7
	7.5		96		161	28.1±1.7
^{27}Al	5.4	85.3	46	272	110	24.3±1.7
	5.9		58		123	27.2±1.7
	6.7		77		142	31.4±1.6
	7.5		97		160	32.6±1.6
^{32}S	5.4	106.3	46	292	110	42.5±2.9
	6.7		83		144	32.2±1.7
	7.5		105		167	41.7±1.5
^{35}Cl	5.4	116.0	49	297	121	52.1±3.0
	5.9		64		135	39.7±1.6
	6.7		88		159	40.1±1.6
	7.5		113		182	44.4±1.7
^{40}Ca	5.0	140.5	31	318		
	5.4		44			
	5.9		62		139	
	6.7		89		164	62.9±1.7
	7.5		116		192	59.0±1.7
^{48}Ca	4.6	166.7	17	315		
	4.8		25			
	5.0		33		102	
	5.4		49		116	
	5.9		69		138	67.4±1.7
	6.7		101		168	63.2±1.7
	7.5		133		198	62.8±1.7
$^{\text{nat}}$Zn	5.4	245.1	27	384		
	6.7		93		205	
	7.5		133		242	

[a] $E^+=E^*+Q_0-\langle E_K\rangle$, where Q_0 is the Q value for symmetric fission of the compound nucleus and $\langle E_K\rangle$ is the experimental total kinetic energy for symmetric fission.

TABLE IV. Parameters and results of the analysis of angular distributions for the ^{238}U+^{16}O,^{26}Mg,^{27}Al reactions.

Reaction	$(E/A)_{\text{lab}}$ (MeV)/nucleon	$E_{\text{c.m.}}$ (MeV)	$T_s{}^{\text{a}}$ (MeV)	$\langle I\rangle$ ($\hbar$)	$\langle I^2\rangle$ ($\hbar^2$)	K_0^{expt} ($\hbar$)	$\left[\frac{\mathcal{J}_0}{\mathcal{J}_{\text{eff}}}\right]^{\text{expt}}$
^{238}U+^{16}O	5.4	81	1.16	15	295	11.1	1.24±0.70
	5.9	88	1.24	26	832	15.5	0.66±0.24
	6.7	100	1.37	30	1079	16.8	0.63±0.28
	7.5	112	1.50	34	1336	18.0	0.60±0.23
^{238}U+^{26}Mg	5.4	127	1.21	32	1272	13.4	0.93±0.30
	5.9	138	1.32	40	1938	17.2	0.61±0.20
	7.5	176	1.61	64	4862	34.3	0.18±0.05
^{238}U+^{27}Al	5.4	131	1.18	32	1218	16.8	0.58±0.40
	5.9	143	1.32	38	1760	14.2	0.90±0.45
	6.7	162	1.49	53	3290	16.1	0.77±0.40
	7.5	182	1.64	60	4252	24.2	0.37±0.30

[a] Nuclear temperature at saddle point $T_s(\text{MeV})=[8.5\times1.02\times(E^*-B_f-\langle E_{\text{rot}}\rangle)/A]^{1/2}$.

guing that the Coriolis forces acting on the system during the descent from saddle to scission are of insufficient strength to change the orientation of the nuclear symmetry axis relative to the total angular momentum vector, which would be required for a change in the K value selected at the saddle point. Recently, it has been suggested that the K distribution may reflect a statistical equilibrium at the scission point, which represents the other extreme for equilibrated K distributions. The variance of the K distribution is in both cases given by the following expression,

$$K_0^2 = \frac{\mathcal{J}_{\rm eff}}{\hbar^2}T, \quad \frac{1}{\mathcal{J}_{\rm eff}} = \frac{1}{\mathcal{J}_{\parallel}} - \frac{1}{\mathcal{J}_{\perp}} , \tag{5}$$

where T is the nuclear temperature, $\mathcal{J}_{\parallel}$ and $\mathcal{J}_{\perp}$ are the moments of inertia for rotations around and perpendicular to the symmetry axis, respectively, all taken at the appropriate point.

The solid curves in Fig. 11 are calculated on the basis of the assumption that the K distribution is determined at the fission saddle point, the shape of which is obtained from the rotating liquid drop model.[21] The dashed curves are based on the assumption that the K distribution reflects the shape of the scission point.[9] Within the rather large error bars, we find that the ^{238}U + ^{16}O data are in good agreement with the saddle point model, and fall significantly outside the expectations of the scission point model. The data for the ^{238}U + ^{27}Al reaction fall in between the predictions for the two models. This behavior is interpreted here as an effect of the significant contribution to the cross section from nonequilibrium quasifission as evidenced by the mass-angle distributions.

In panel (c) of Fig. 10 we show the angular distribution for fragments heavier than symmetry only. One sees a distinct forward-backward asymmetry, which is incompatible with compound nucleus fission. The solid curves are fitted to the backward part of the distribution only, under the extreme assumption that this component is the one that is associated with compound fission. The resulting variances of the K distributions are shown as open symbols in Fig. 11(c). The fact that also these values deviate from the saddle point estimate suggests that some fraction of the backward cross section is associated with quasifission as well.

E. Signatures for quasifission

In the preceding subsections we have presented several observations, which have been interpreted as manifestations of the quasifission process. These signatures may be summarized as follows:

(i) Large mass widths, incompatible with compound nucleus fission.

(ii) Asymmetries in the mass-angle correlation of fragments.

(iii) Large angular anisotropies, incompatible with compound nucleus fission.

These signatures have been observed earlier in separate experiments.[1-13] In the present study, they are observed simultaneously, giving strong evidence that these signatures, in fact, reflect different aspects of the same process, i.e., quasifission. The first two signatures are associated with the degree of relaxation in the mass asymmetry achieved within the time available for the reaction, whereas the latter is associated with the shape and degree of K equilibration of the intermediate system. As a result, the occurrence of quasifission can be recognized from the angular distribution even when long reaction times allow the mass drift toward symmetry to be completed. The ^{238}U + ^{26}Mg reaction is an example of this. It shows only a marginal increase in the mass width and has symmetric mass-angle correlations. The angular anisotropy is, however, significantly larger than expected for compound nucleus fission, suggesting that a significant fraction of the capture cross section arises from quasifission.

F. Capture cross sections

The total capture cross sections were obtained on the basis of the plots of total kinetic energy versus fragment mass as shown in Figs. 3 and 4. The separation between capture and scattering events is very pronounced for the lighter targets, ^{16}O to ^{32}S, but becomes slightly less evident for heavier targets. The separation that has been chosen between the two components for these targets is indicated by dotted lines. The cross sections obtained by integrating over the capture component are then corrected for losses arising from detection inefficiencies near the beam axis and sequential fission of heavy reaction partners. The results are shown as solid points in Figs. 12 and 13, and listed in Table II. The capture cross sections will be discussed in detail in Sec. IV.

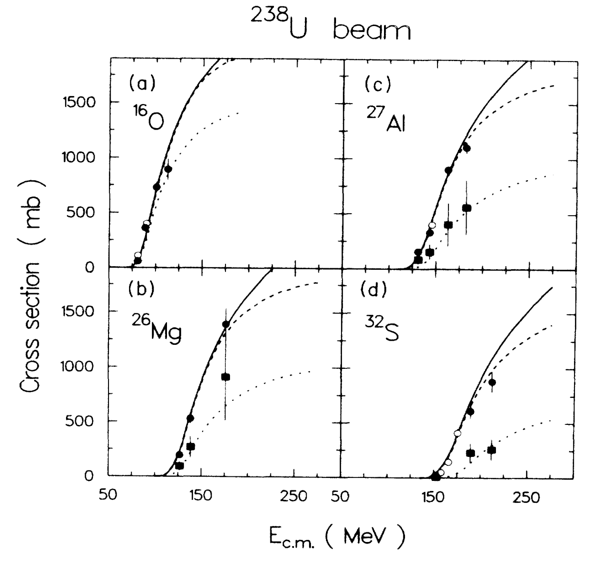

FIG. 12. Cross sections for fission-like processes are shown as solid circles for the reactions ^{238}U+^{16}O, ^{26}Mg, ^{27}Al, and ^{32}S as a function of the center-of-mass energy $E_{\rm c.m.}$ in panels (a), (b), (c), and (d), respectively. Open circles are taken from Refs. 13 and 55. The solid squares represent the cross section for complete fusion followed by fission. The solid, dashed, and dotted lines represent theoretical predictions of the cross section for touching, capture, and complete fusion processes, respectively.

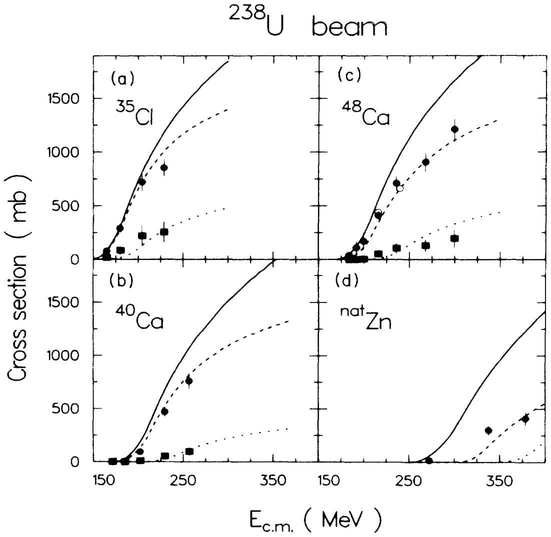

FIG. 13. Same as for Fig. 12 for the reactions $^{238}U+^{35}Cl$, ^{40}Ca, ^{48}Ca, and ^{nat}Zn.

G. Complete fusion cross sections

The separation of the capture cross section into complete fusion and quasifission components is less straightforward than in the case of capture and scattering reactions. Although several distinctive features of quasifission have been identified as discussed in the preceding subsection, they cannot be utilized unambiguously in a quantitative analysis. Additional simplifying assumptions are required.

As a first step we estimate the complete fusion cross section on the basis of the mass spectra by requiring that (1) the complete fusion component is symmetric and has the expected mass width, and (2) that only a fraction of the cross section at mass symmetry is associated with complete fusion. This fraction is 100% for the ^{16}O target decreasing to about 40% for ^{48}Ca. The estimates of these fractions are based on extrapolations from a quantitative analysis of the angular anisotropies.[9] The mass distribution for fission of a completely fused system is assumed to be a Gaussian centered at symmetry with a variance given by Eq. (2).

As a second step these estimates have been compared with simulations[22] of the mass-angle correlations, in which the mass drift toward symmetry during the rotation of the intermediate complex as a whole have been calculated under simplifying assumptions in order to compare with the measured mass-angle correlations. The main assumptions are that a definite l value (to be determined) separates complete fusion from quasifission. The lower l values lead to complete fusion, followed by isotropic emission of fission fragments (i.e., large K_0/l ratio), with a mass width according to Eq. (2). Higher l-values up to l_c^{expt} give rise to double trapezoidal mass distributions of quasifission products. They change smoothly with target Z value and bombarding energy, reflecting a tendency for more asymmetric quasifission with lighter Z value, higher l value, and lower bombarding energy. The trapezoidal distributions are further convoluted with mass widths that approach the limit of Eq. (2) for symmetric masses, and they are normalized to the measured cross section for capture (minus complete fusion). For each value of the mass asymmetry there is a definite reaction time [see Sec. V, Fig. 19 and Eq. (28)], l value, and moment of inertia, and thus a definite turning angle during the reaction. This angle is given a distribution with a width that increases with the square root of the turning angle. The decay into two quasifission fragments is further assumed to occur in a direction perpendicular to the total angular momentum vector, corresponding to $K_0=0$. When these simulated mass-angle distributions are required to look like the experimental ones as shown in Figs. 5 and 6, one obtains a sensitive estimate of the component of complete fusion present in the experimental distributions. This simulation technique results in complete fusion cross sections, which are in agreement with those obtained from the former method to within better than about 30–50 % for the heavy targets, and considerably better for the lightest targets. We consider 30–50 % to be the accuracy with which complete fusion cross sections can be determined from the present data.

The results are summarized in Table V and shown as solid squares in Figs. 12 and 13. We observe that for the

TABLE V. Complete fusion cross sections and extra-extra push energies. ΔE is the extra energy needed for complete fusion. It is extracted from the experimental compound nucleus formation cross section (see text). $E_{xx}(l=0)$ is the extra-extra-push energy for the central collision.

Target	$(E/A)_{\text{lab}}$ (MeV/nucleon)	σ_{CF} (mb)	ΔE (MeV)	$E_{xx}(l=0)$ (MeV)
^{26}Mg	5.4	95±30	7	7±4
	5.9	270±80	9	
	7.5	910±300	19	
^{27}Al	5.4	85±30	2	1±3
	5.9	155±50	9	
	6.7	405±120	17	
	7.5	560±180	28	
^{32}S	5.4	5.4±1.6	7	6±4
	6.7	230±80	20	
	7.5	260±100	40	
^{35}Cl	5.4	16±5	8	9±4
	5.9	85±30	14	
	6.7	220±80	27	
	7.5	255±90	48	
^{40}Ca	5.0	0.11±0.06		28±8
	5.4	1.1±0.5		
	5.9	10.6±4	20	
	6.7	54±20	38	
	7.5	98±40	59	
^{48}Ca	4.6	0.06±0.03		25±8
	4.8	0.5±0.2		
	5.0	4.5±2.0	24	
	5.4	53±20	30	
	5.9	105±40	43	
	6.7	130±50	72	
	7.5	195±90	96	

heavy targets only a very small fraction of the capture cross section can be attributed to complete fusion between target and projectile. This indicates that a large additional energy, over and above the interaction barrier and above the extra energy required for capture, must be provided to the system in order to initiate complete fusion. The shapes of the excitation functions are indicative of a dynamical hindrance of complete fusion. It will be discussed in the framework of the extra push model in the following section.

IV. DISCUSSION OF CAPTURE AND COMPLETE FUSION

In reactions with "light" heavy ions it is sufficient to provide a radial energy equal to the one-dimensional interaction barrier in order to achieve complete fusion of the target and projectile. The complete fusion cross section at a particular bombarding energy may therefore be determined from the highest partial wave for which the sharing of the center of mass energy between radial and tangential motion leaves sufficient radial energy to fulfill this condition. This gives rise to the following approximate expression for the complete fusion cross section,

$$\sigma_t = \pi R_I^2 (1 - V_I / E_{\text{c.m.}}) , \qquad (6)$$

where V_I and R_I are the interaction barrier height and radius, respectively. From systematic studies of a very large set of experimental complete fusion cross sections it has been found[23,24] that the interaction barrier is slightly overpredicted by the nuclear proximity potential[25] calculated using standard liquid drop model[26] parameters. This discrepancy can be removed[13] by using parameters relating to the nuclear surface tension obtained in a model using a folded Yukawa force[27] and adjusted to experimental nuclear masses and radii. In the following we shall use interaction barriers obtained in this manner. It has also been pointed out in several studies[28-32] that the so called sharp cutoff model represented by Eq. (6) severely underpredicts the complete fusion cross section at energies near, and in particular, below the interaction barrier V_I. In light systems, a fraction of this enhancement arises from quantum-mechanical tunneling of the interaction barrier, but in heavier systems the enhancement is mainly due to barrier fluctuations arising from static target deformations[28] and surface vibrations[32] of the interacting nuclei. In the present work we have taken both of these effects into account, the details of the calculations being described in Ref. 10.

A. Extra-push scaling law for capture

The experimental capture cross sections are shown as solid circles in Figs. 12 and 13. The solid curves represent the theoretical touching cross section calculated according to the procedure outlined above. We observe that the capture cross section is of the same magnitude as the theoretical touching cross section for the ^{16}O and ^{26}Mg targets, as well as the lowest energy points for the ^{27}Al and ^{32}S and ^{35}Cl targets. At the highest energies we observe a clear cross section deficiency for targets heavier than ^{27}Al. This indicates that it is not sufficient to overcome the interaction barrier in order to achieve capture in these systems. An additional energy, the extra push energy, E_x, is needed to obtain capture for the highest partial waves. This extra push energy may be read directly off the figures as the additional energy needed to achieve a certain cross section level, allowing for the $1/E_{\text{c.m.}}$ reduction of the cross section corresponding to a specific maximum partial wave, i.e.,

$$E_x = E_c - E_t ,$$

where

$$E_t = E_c \sigma_c(E_c) / \sigma_t(E_t) . \qquad (7)$$

Here, σ_t and σ_c refer to the calculated touching cross section and the experimental capture cross section, respectively. For each data point showing a cross section deficiency the extra push energy has been determined in this manner.

In keeping with the extra push model,[33,34] we may express the extra push energy as follows,

$$E_x = E_{\text{ch}} a^2 (x'_{\text{Bass}} - x_{\text{th}})^2 , \qquad (8)$$

where E_{ch} is a characteristic energy, a is the slope coefficient, and x'_{Bass} is an effective fissility parameter reflecting the relative strength of repulsive and attractive forces of the entrance channel system. The characteristic energy is given by

$$E_{\text{ch}} = \frac{2048}{81} \left[\frac{\pi}{3} \right]^{4/3} \left[\frac{m\gamma^2 r_0^6}{\hbar^2} \right] \frac{A_1^{1/3} A_2^{1/3} (A_1^{1/3} + A_2^{1/3})^2}{A} , \qquad (9)$$

where m is the atomic mass unit, γ is the surface tension coefficient, and r_0 is the radius parameter. The effective fissility parameter is given by

$$x'_{\text{Bass}} = 1.2 \frac{F_{\text{Coul}} + F_{\text{cent}}}{(F_{\text{nucl}})_{\text{max}}} , \qquad (10)$$

where F_{Coul}, F_{cent}, and $(F_{\text{nucl}})_{\text{max}}$ is the Coulomb, centrifugal, and nuclear force, respectively, at the point of maximum nuclear attraction.

For the interaction between spherical nuclei, we may write

$$\begin{aligned} F_{\text{Coul}} &= Z_1 Z_2 e^2 / r_m^2 , \\ F_{\text{cent}} &= (fl)^2 \hbar^2 / \mu r_m^3 , \\ (F_{\text{nucl}})_{\text{max}} &= 4\pi\gamma\bar{c}\phi_{\text{max}} , \end{aligned} \qquad (11)$$

where the nuclear force is obtained on the basis of the proximity model. In this model the maximum nuclear attraction is achieved at an internuclear distance of $r_m = c_1 + c_2 + 0.3$ fm, where the c_i, $i = 1,2$, refer to the central radii of the interacting nuclei. At this distance the proximity function assumes a value of $\phi_{\text{max}} = 0.9601$. Inserting these expressions into Eq. (10), we find

$$x'_{\text{Bass}} = x'_{\text{Bass}}(l=0) + f^2 (l / l_{\text{ch}})^2 , \qquad (12)$$

where f is the fraction of the total angular momentum, l, which remains in orbital motion. The characteristic angu-

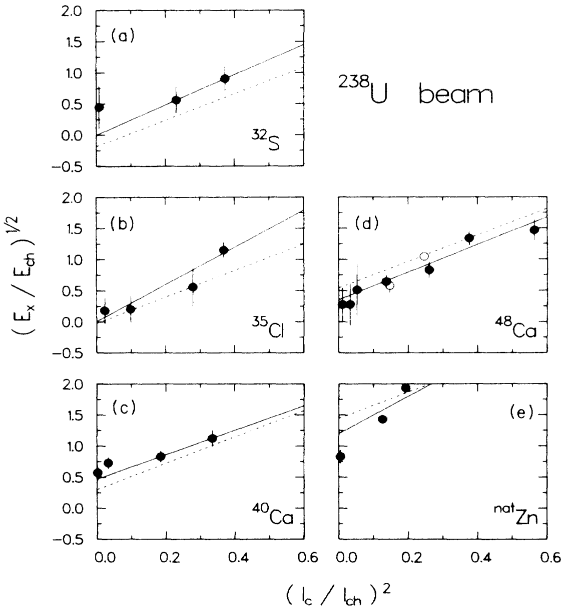

FIG. 14. Solid points represent experimental values of the parameter $(E_x/E_{ch})^{1/2}$ for the reactions ^{238}U+^{32}S, ^{35}Cl, ^{40}Ca, ^{48}Ca, and ^{nat}Zn shown as a function of the parameter $(l_c/l_{ch})^2$ in panels (a), (b), (c), (d), and (e), respectively. Open points are obtained from Ref. 13. Solid lines are fits to the data points. Dashed lines represent the prediction based on the overall systematics.

lar momentum, l_{ch}, is given by

$$l_{ch}=(10\pi\gamma\bar{c}\phi_{max}\mu r_m^3/3\hbar^2)^{1/2}\ , \tag{13}$$

where μ is the reduced mass in the entrance channel.

Guided by the scaling properties of Eq. (10), we plot the quantity $(E_x/E_{ch})^{1/2}$ against $(l_c/l_{ch})^2$ for the experimental data points in Fig. 14. The limiting angular momentum for capture, l_c, is derived from the experimental cross section on the basis of a sharp cutoff approximation. We notice that the data points exhibit the expected linear dependence between the two quantities supporting the extra push model.

B. Influence of N/Z equilibration

The extra push energy for central collisions are obtained from the data by extrapolation along the solid lines to $l_c=0$. The scaling properties of the extra push model may be tested by plotting the resulting values of $(E_x/E_{ch})^{1/2}$ as a function of either the effective fissility x_{eff}, Fig. 15(a), or the parameter x'_{Bass}, Fig. 15(c). The effective fissility parameter

$$x_{eff}=1.2F_{Coul}/(F_{nucl})_{max} \tag{14}$$

scales with the force balance between the interacting nuclei, assuming spherical shapes with sharp surfaces, whereas the parameter x'_{Bass} reflects the same quantity, but calculated assuming diffuse nuclear surfaces and modified values of the nuclear radii and surface tension coefficient. A comparison of the effective fissility parameters is listed in Table VI. These modifications result in a better representation of the interaction barrier heights, as discussed in Sec. IV. Furthermore, this redefinition of the scaling parameter allows for a generalization of the extra push concept to nonspherical interacting nuclei, which becomes very important at near and subbarrier energies.

In Figs. 15(a) and 15(c) we have also included experimental estimates of the extra push energy for head-on collisions for several other reactions[11,13,35,36] and we find a reasonable overall linear scaling with either of the effective fissility parameters. There appears, however, to be a slight discrepancy between the results for very asymmetric reactions, such as those studied in the present work, and the nearly symmetric reactions of Ref. 35 and 36. The threshold values of the effective fissility, x_{eff}, or x'_{Bass}, are significantly different. In agreement with earlier studies,[11,13] a threshold value of $x_{th}=0.7$ is obtained for the

TABLE VI. Comparison of different fissility parameters. The columns (1–5) give the following quantities: (1) $x'_{Bass}=1.2[F_{Coul}(r_m)+F_{cent}(r_m)]/F_{nucl}(r_m)$, $r_m=c_1+c_2+0.3$ fm. r_m is the point of maximum nuclear attraction, $F_{nucl}(r_m)=4\pi\gamma\bar{c}\phi_{max}$, $c_i=R_i-b^2/R_i$, $R_i=1.28A_i^{1/3}-0.76+0.8A_i^{-1/3}$, $b=1$ fm, $\bar{c}=c_1c_2/(c_1+c_2)$, $\gamma=\gamma_0(1-2.3I^2)$, and $\phi_{max}=0.9601$, $\gamma=1.2496$ MeV fm^{-2}. (2) $(x'_{Bass})_{eq}$ is the system parameter after N/Z equilibrium. Keeping the mass constant, the formulae $Z'_T=A_T(Z/A)$, $N'_T=A_T-Z'_T$ give the proton and neutron number in the nucleus after N/Z equilibrium. (3) $x_e=(Z^2/A)_{eff}/(Z^2/A)_{crit}$, $(Z^2/A)_{eff}=4Z_1Z_2/[A_1^{1/3}A_2^{1/3}(A_1^{1/3}+A_2^{1/3})]$, $(Z^2/A)_{crit}=50.9(1-1.78I^2)$, $I=(N-Z)/A$. (4) $(x_e)_{eq}$ is the effective system parameter after N/Z equilibrium. (5) $x=(Z^2/A)/(Z^2/A)_{crit}$.

	Entrance channel				Composite system	
Target	x'_{Bass}	$(x'_{Bass})_{eq}$	x_e	$(x_e)_{eq}$	$^{A}_{Z}$X	x
^{16}O	0.532	0.426	0.462	0.370	$^{254}_{100}$Fm	0.841
^{26}Mg	0.610	0.501	0.561	0.486	$^{264}_{104}$X	0.895
^{27}Al	0.644	0.543	0.595	0.502	$^{265}_{105}$X	0.885
^{32}S	0.717	0.593	0.675	0.559	$^{270}_{108}$X	0.914
^{35}Cl	0.727	0.690	0.690	0.586	$^{273}_{109}$X	0.922
^{40}Ca	0.790	0.663	0.760	0.638	$^{278}_{112}$X	0.950
^{48}Ca	0.733	0.698	0.713	0.679	$^{286}_{112}$X	0.940
^{nat}Zn	0.918	0.826	0.918	0.827	$^{302}_{122}$X	1.036

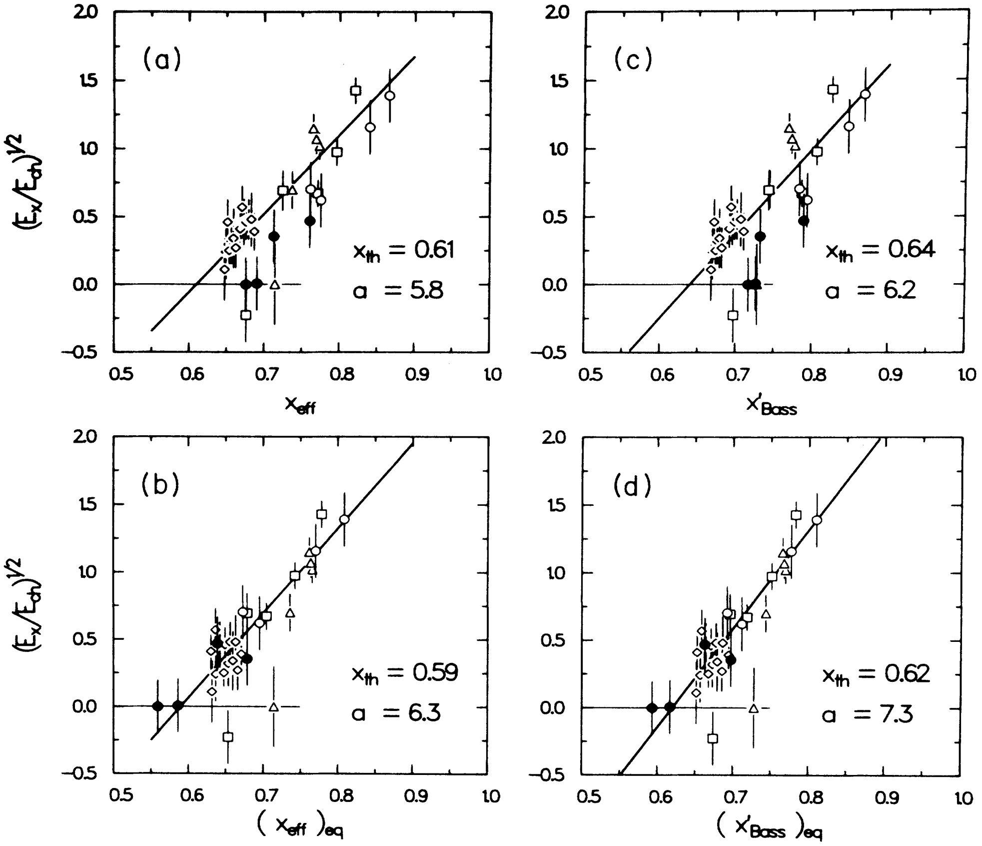

FIG. 15. The parameter $(E_x/E_{ch})^{1/2}$ is plotted against the four scaling parameters, x_{eff}, $(x_{eff})_{eq}$, x'_{Bass}, and $(x'_{Bass})_{eq}$ in panels (a), (b), (c), and (d), respectively. Solid points are obtained from the present work, whereas open circles, open squares, open triangles, and open diamonds are from Refs. 13, 11, 35, and 36, respectively. The thick solid lines represent the best fits to the data, the parameters of which are indicated in the figure.

reactions with mass asymmetric entrance channels, whereas the data for more symmetric reactions[36] indicate a threshold value of $x_{th}=0.61-0.64$.

A possible cause of this inconsistency may be found in the rapid equilibration of the isospin mode during the early stages of the reaction. Studies of deeply inelastic and quasielastic scattering show[37] that this mode is nearly completely equilibrated in the early stages of the reactions. We have therefore examined the scaling properties of the extra-push energy with respect to the effective fissility parameters, $(x_{eff})_{eq}$ and $(x'_{Bass})_{eq}$, referring to charge equilibrated systems as shown in Figs. 15(b) and 15(d), respectively. These parameters are calculated assuming that the total charge is distributed according to the mass of the interacting nuclei while the initial mass asymmetry is preserved. We observe that most of the above mentioned discrepancy between mass asymmetric and symmetric systems is removed under this assumption, although a few points, notably the ^{208}Pb + ^{48}Ca and ^{90}Zr + ^{90}Zr, fall outside the systematic trend. It is reasonable to expect that this particular deviation is caused by the especially strong shell effects in these systems. Otherwise we find a good universal correlation between the experimental extra push and the charge equilibrated effective fissility parameters. From this analysis one obtains, however, significantly different threshold and slope parameters compared to earlier analysis in which no charge equilibration was assumed.

The increase in the quantity $(E_x/E_{ch})^{1/2}$ with $(l_c/l_{ch})^2$ as illustrated in Fig. 14 is related to the l dependence of the effective fissility, Eqs. (8) and (12), the slope being af^2. Having determined the quantity a from the scaling properties of the extra push energy, $a=7.3\pm1.0$, we may obtain an estimate of the angular momentum fraction, f. There is no reason to expect that this quantity should be strictly constant, but we find that a constant value of $f=0.55$ is in reasonable agreement with the experiment, as illustrated by the dashed lines in Fig. 14. These lines are drawn on the basis of the effective fissility parameter, $(x'_{Bass})_{eq}$, using a threshold value of $x_{th}=0.62$ and a slope of $a=7.3$. For ease of calculation, we therefore assume f to be constant in the following.

C. Complete fusion and the extra-extra push

The complete fusion cross sections estimated on the basis of the measured fragment mass distributions according to the methods described in Sec. III G are shown as solid squares in Figs. 12 and 13 and listed in Table V. We observe that the complete fusion cross section constitutes only a small fraction of the capture cross section, especially for the heavier targets. This implies that a radial energy, E_{xx}, may be needed in excess of the interaction barrier, V_I, and E_x in order to lead to complete fusion of the system. Since the complete fusion cross section is always smaller or equal to the capture cross section, it follows that this extra-extra push energy is larger or equal to the extra-push energy needed to induce capture. From the experimental data we may estimate the extra-extra push energy in a manner analogous to the estimate of the extra-push energy from the capture cross section. Thus we have

$$E_{xx} = E_{\mathrm{CF}} - E_t \ , \tag{15}$$

where

$$\sigma_t = \sigma_{\mathrm{CF}}(E_{\mathrm{CF}}/E_t) \ ,$$

Here, σ_t and σ_{CF} refer to the calculated touching cross section and the experimental complete fusion cross section, respectively.

The extra-extra push energy, E_{xx}, is expected to be given by

$$E_{xx} = E_{\mathrm{ch}} a^2 (x_m - x_{\mathrm{th}})^2 \ , \tag{16}$$

where x_m is a scaling parameter composed of the effective fissility and the true fissility of the system as defined below. The characteristic energy, E_{ch}, is defined in Eq. (9) and listed in Table VII for the reactions studied in the present work. The slope parameter, a, and the threshold, x_{th}, are determined from the data.

It has been suggested[34] tentatively that the mean fissility parameter, x_m, is the geometrical mean between the effective fissility, x_{eff}, which reflects the force balance in the entrance channel, and the true fissility, x, related to the stability against fission of a spherical compound system. It was furthermore assumed that a simple l^2 term accounts for the increased hindrance of complete fusion with angular momentum.[34,9] In a recent theoretical study[38] of the dynamical scaling properties of the extra-push model, it has been suggested that the mean fissility, x_m, may be better represented by the more general form

$$x_m = x_{\mathrm{eff}}^{\mu} x^{1-\mu} \ , \tag{17}$$

where dynamical equivalence was found for different systems with the same value of x_m if a value of $\mu = 0.71$ was used. In the analysis of the present data, and other data found in the literature, we have used this form of the mean fissility. The relative weighting between the effective fissility x_{eff} and the true fissility x expressed by the exponent μ was, however, allowed to assume a value different from 0.71 in order to obtain the optimal representation of the data. Assuming that the mean fissility increases approximate linearly with l_{CF}^2 we plot the quantity $(E_{xx}/E_{\mathrm{ch}})^{1/2}$ as a function of l_{CF}^2 in Fig. 16 for the data obtained in the present experiment. Here, l_{CF} represents the highest partial wave leading to complete fusion, estimated from the experimental cross section on the basis of the sharp cutoff assumption. The thick lines represent the estimated best fits to the data points under the constraint of reasonable f values, i.e., $f \approx 0.55$. The intercepts of these lines with the ordinate represents the experimental estimates of $(E_{xx}/E_{\mathrm{ch}})^{1/2}$ for head-on collisions, i.e., the extra-extra push energy needed to achieve complete fusion in this situation.

TABLE VII. Extra push parameters.

Reaction	E_{ch} (MeV)	$l_{\mathrm{ch}}(\hbar)$
^{238}U+^{16}O	9.2	92.1
^{238}U+^{26}Mg	11.5	135.4
^{238}U+^{27}Al	11.8	139.8
^{238}U+^{32}S	12.9	160.3
^{238}U+^{35}Cl	13.4	171.7
^{238}U+^{40}Ca	14.4	190.7
^{238}U+^{48}Ca	14.8	216.7
^{238}U+^{64}Zr	17.5	272.0

In order to study the scaling properties of the extra-extra push energy, we have plotted the quantity $(E_{xx}/E_{\mathrm{ch}})^{1/2}$ as a function of the mean fissility parameter, $(x'_{\mathrm{Bass}})_{\mathrm{eq}}^{\mu} x^{1-\mu}$, for three different values of μ, in Fig. 17. We have chosen to use the charge equilibrated effective fissility parameter for diffuse surface nuclei $(x'_{\mathrm{Bass}})_{\mathrm{eq}}$ for the reasons mentioned in Sec. IV B. The solid points are from the present study, open circles are obtained from an analysis of fission fragment angular distributions,[9] and the open squares are obtained from an analysis of evaporation residue cross sections for nearly symmetric systems.[35] From Fig. 17(a) we observe a substantial discrepancy between symmetric and asymmetric systems if scaling with either the effective fissility $(x'_{\mathrm{Bass}})_{\mathrm{eq}}$ or the true fissility x is attempted. We find, however, that a mean fissility parameter of

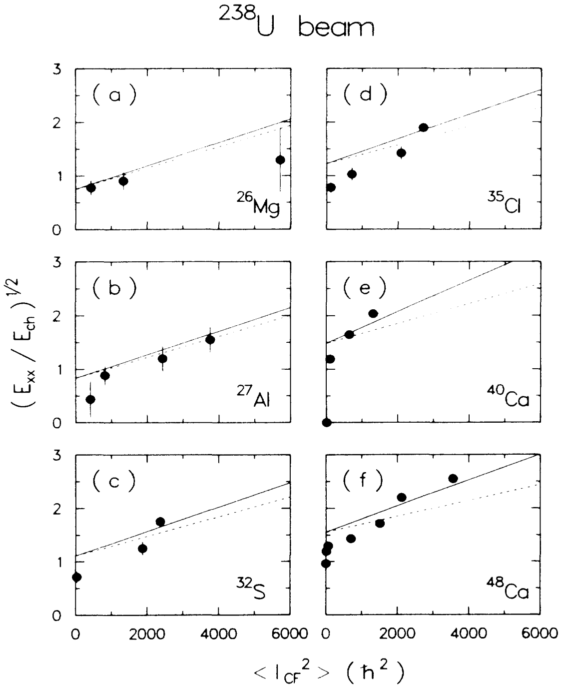

FIG. 16. Solid points represent experimental values of the parameter $(E_{xx}/E_{\mathrm{ch}})^{1/2}$ for the reactions ^{238}U+^{26}Mg, ^{27}Al, ^{32}S, ^{35}Cl, ^{40}Ca, and ^{48}Ca shown as a function of the parameter l_{CF}^2 in panels (a), (b), (c), (d), (e), and (f), respectively. The solid lines are fits to the data points using Eqs. (16) and (20). Dashed lines represent the l dependence based on Eq. (19).

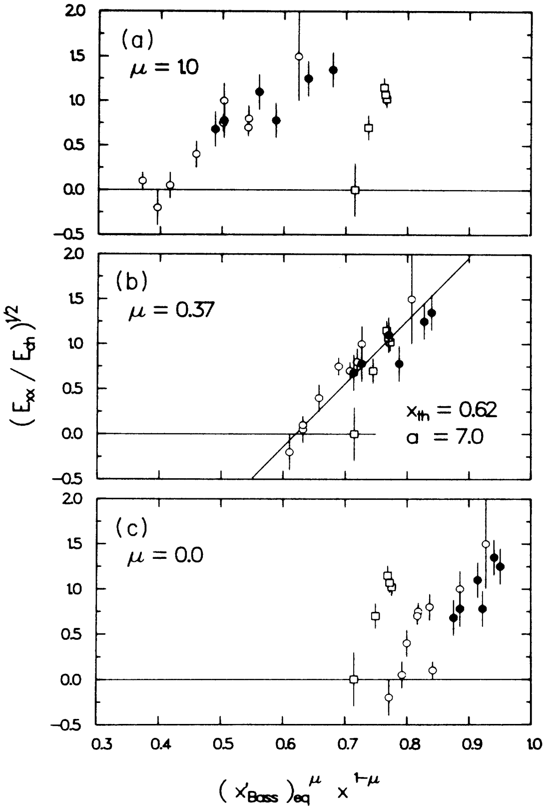

FIG. 17. The parameter $(E_{xx}/E_{\rm ch})^{1/2}$ is plotted against the scaling parameter $(x'_{\rm Bass})^{\mu}_{\rm eq}x^{1-\mu}$ for three values of μ, 1.0, 0.37, and 0.0, in panels (a), (b), and (c), respectively. The solid points are obtained from the present work, whereas open circles and open squares are from Refs. 9 and 35, respectively. The solid line in panel (b) represents the best fit to the data, the parameters of which are indicated in the figure.

$$x_m=(x'_{\rm Bass})^{0.37}_{\rm eq}x^{0.63}\ , \tag{18}$$

i.e., $\mu=0.37$, constitutes a reasonable scaling parameter for the extra-extra push energy. As is the case for the systematics of the extra push energy, we find that the ^{90}Zr + ^{90}Zr point [open square at $(E_{xx}/E_{\rm ch})^{1/2}=0$] falls outside the general trend. Again, it may be argued that this discrepancy is associated with the unusual strong binding of both reaction partners in this case. The resulting threshold and slope parameters, $x_{\rm th}=0.62\pm0.03$ and $a=7\pm1$, are in good agreement with the previous estimates obtained from a smaller subset of the data excluding the data from the present study.

The value of $\mu=0.37$ resulting from this analysis seems to suggest that the properties of the compound system are more important than estimated on the basis of the theoretical studies.[38] Although this discrepancy is not understood at present, it may indicate that the numerous simplifications assumed with this model lead to numerical inaccuracies.

An important result of the present analysis is the fact that identical values of the threshold fissility, $x_{\rm th}$, and the slope parameter, a, are obtained from the analysis of both the experimental capture cross sections and complete fusion cross sections, removing an earlier discrepancy and establishing consistency with central aspects of the theoretical extra push model. This is mainly a result of taking fast charge equilibration in the entrance channel into account in the calculation of the effective fissility parameter.

The l dependence of the mean fissility has been suggested[34] to be given as a simple linear dependence of $l^2_{\rm CF}$ according to

$$x_m(l)=x_m(l=0)+f(l/l''_{\rm ch})^2\ , \tag{19}$$

where

$$l''_{\rm ch}=(l_{\rm ch}l_{B_f=0})^{1/2}/(1-x)^{1/4}\ ,$$

and f is the angular momentum fraction, see Eq. (11). In the above expression, $l_{\rm ch}$ is the characteristic angular momentum for capture given by Eq. (13), $l_{B_f=0}$ is the angular momentum at which the fission barrier vanishes according to the rotating liquid drop model,[21] and x is the fissility parameter.

The l dependence of x_m according to Eq. (19) (dashed lines) is compared with the experimental data, $x_m(l=0)$ being given by Eq. (18). We find that the increase in E_{xx} with spin is not as steep as indicated by the experimental data, especially for the heavier targets. A slightly better agreement with the data is obtained if the following relation is used,

$$x_m(l)=(x'_{\rm Bass})_{\rm eq}(l)^{0.37}x(l)^{0.63}\ , \tag{20}$$

where

$$x(l)=x(l=0)+(1-x)(l/l_{B_f=0})^2\ .$$

Using this l dependence results in a somewhat stronger increase in the extra-extra push energy with spin, as represented by the solid lines in Fig. 16. The angular momentum fraction used in these estimates is identical to the value used to estimate the capture cross section, namely $f=0.55$.

D. Model calculations

Having determined the parameters for the extra-push model as detailed above, it is of interest to perform actual calculations of the cross sections for capture and complete fusion for comparison with the experimental quantities. Insofar as the parameters are extracted from the experimental estimates of the extra- and extra-extra-push energies, it is expected that the model calculations will provide a good representation of the experimental cross sections. There are, however, several approximations in the determination of the extra- and extra-extra-push energies from the cross sections which may modify this expected agreement. One of these is the assumption of a sharp cutoff in the l distributions for both capture and complete fusion. The cross section calculations take into account both the barrier fluctuation caused by target deformation and zero-point vibration,[10,13] as well as the effect of quantum-mechanical tunneling through the interaction barrier. Both of these effects cooperate to produce smooth l distributions, as opposed to the sharp cutoff assumption used in the first analysis. These barrier fluctuations are propagated to the capture and complete fusion cross section.

E. Extra push fluctuations

Recently, it has been observed[39,40] that the complete fusion cross sections vary even more smoothly for energies near threshold than what can be accounted for by the interaction barrier fluctuations. This effect has been attributed to fluctuations in the extra-extra push energy needed to bring the system from the configuration of the interaction barrier to a configuration inside the true saddle point (the fission barrier). Since this motion is subject to a substantial dissipation, it is natural to expect that it is associated with a certain amount of fluctuations. In the present treatment we have assumed that the extra-extra push energy required to bring the system to a configuration behind the true saddle point has a Gaussian distribution, i.e.,

$$\rho(E_{xx})=\exp\{[E_{xx}-E_{xx}(0)]^2/2\sigma_{xx}^2\} , \tag{21}$$

where

$$\sigma_{xx}^2=\sigma_0 E_{xx}(0) . \tag{22}$$

In this expression it is assumed that the variance increases linearly with the extra-extra push energy, as would be the case in a multistep process. The constant σ_0 is to be determined from the near barrier behavior of the excitation function for complete fusion. In Fig. 18 the effect of the fluctuations in the extra-extra push energy is illustrated for the $^{238}\mathrm{U}+{}^{48}\mathrm{Ca}$ reaction. The solid circles represent the experimental complete fusion cross sections obtained in the present work as detailed in Sec. III G. The solid curve represents extra push model calculations of the complete fusion cross section following the guidelines of the preceding section including barrier fluctuations. This calculation is carried out using standard parameters, $\sigma_0=2$ MeV, $x_{\mathrm{th}}=0.62$, $a_{xx}=7$, $f=0.55$, and $\mu=0.37$, whereas a calculation of the complete fusion cross section in which the fluctuation of the extra-extra push energy is disregarded (i.e., $\sigma_0=0$) is illustrated by the dotted curve. We observe that this latter calculation severely underestimates the complete fusion cross section at near barrier energies by falling off much more rapidly when approaching the barrier energy than seen in the experimental data. This effect is taken in support of the assumption of a fluctuating extra-extra push energy as described above.

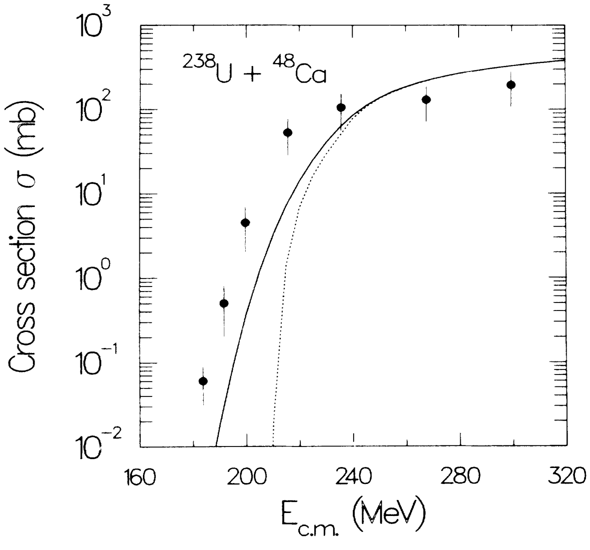

FIG. 18. Illustration of the effect of extra-extra push fluctuations. Excitation functions for complete fusion calculated with (solid curve) and without (dashed curve) extra-push energy fluctuation are compared with the experimental data for the $^{238}\mathrm{U}+{}^{48}\mathrm{Ca}$ system.

F. Summing up

The analysis carried out in the present section is based on the most comprehensive and diverse set of experimental results used so far to assess the qualitative and quantitative validity of the extra push model.

The prominent qualitative feature of this model[33] is that the motion inside the touching barrier is highly dissipative, being dominated by dinuclear and mononuclear one-body friction, while the conservative driving forces are of liquid drop type. This leads to the specific scaling laws that further require identical threshold and slope parameters for capture and complete fusion reactions. We have shown that the experimental results qualitatively reflect the scaling laws of the prescribed type with equal threshold and slope parameters for the two kinds of reactions. The existence of such systematic correlations between quite diverse measurements lends strong support to the validity of the central assumptions of the theory.[33]

Quantitatively, the extracted parameters $x_{\mathrm{th}}=0.62$ and $a_x=a_{xx}=7$ can be compared to theoretical model calculations[41] of central collisions leading to the same reactions, using sharp surface model-nuclei and shapes described by three parameters only (elongation, neck radius, and mass asymmetry). The corresponding theoretical parameters are $x_{\mathrm{th}}=0.723$ and $a_x=a_{xx}=18$. A discrepancy between theory and experiment of this magnitude certainly cannot be neglected. It remains to be seen whether or not it can be understood as a result of surface diffuseness and (dissipative) fluctuations or in terms of shapes that so far have been neglected in the theoretical model calculations. It is also possible that the procedures used to separate mean values from fluctuation effects in the analysis of the experimental data tend to result in a lowering of the extracted threshold and slope parameters without affecting the scaling behavior.

V. DISCUSSION OF MASS DRIFT TOWARD SYMMETRY

A. General properties

In the past the deep inelastic scattering process has provided most of our knowledge on mass rearrangements in heavy ion reactions. The deeply inelastic scattering process was found to be associated with an unexpectedly small net mass transfers between the reaction partners, although a pronounced increase in mass width as a function of the energy dissipation in the process has been observed and studied in great detail. In these studies one has also observed a net change in the element distribution without an associated drift in the average fragment mass consistent with a fast equilibration of the isospin mode during the short reaction time (typically, $\tau \sim 1\times 10^{-21}$ s).

In contrast to these observations, we find a large degree of mass drift for the completely damped processes, i.e., reactions in which the total kinetic energy in the exit channel can be thought of as representing the Coulomb repulsion between the final fragments at the point of scission according to the Viola systematics.[17] One finds that mass drift toward symmetry takes place only in reactions where the relative motion of the interacting nuclei has been completely damped.

By studying the fragment mass-angle correlations shown in Figs. 5 and 6, we observe that the mass drift toward symmetry is often incomplete. The mass-angle correlation for the ^{238}U + ^{16}O reaction is, however (within experimental uncertainties), perfectly reflection symmetric around the $\theta_{\mathrm{c.m.}}=90^\circ$ line and around mass symmetry at $A=127$ u. This behavior is expected (and required) for the decay of a compound nucleus by virtue of the hypothesis of independence between formation and decay. For reactions on targets heavier than ^{26}Mg we observe a progressive deviation from these symmetries, which indicates the presence of non-compound-nucleus reactions with time scales that are short compared with the characteristic time scale for mass drift all the way to symmetry. Due to its distinctive characteristics, this class of processes is referred to as quasifission reactions. They may be viewed as the connecting link between partially damped deeply inelastic processes and complete fusion, its main distinction being a completely damped kinetic energy in the exit channel combined with various degrees of mass drift toward symmetry.

B. Angles of rotation—reaction times

Aside from the mere observation that the mass-angle correlations for targets heavier that $A\sim 27$ are inconsistent with the fission decay of a compound nucleus, we will in the present subsection attempt to estimate the reaction times for such processes from the observed emission angles and estimated mean angular momenta.

The angle of rotation of the intermediate system is

$$\Delta\theta=\pi-\theta_i-\theta_f-\theta \ , \tag{23}$$

where θ is the observed scattering angle and θ_i and θ_f are half of the computed Coulomb deflection angles of initial and final trajectories.[42] The reaction time, i.e., the period during which the nuclear interaction between the two reaction partners is significant, is given by

$$t_{\mathrm{reac}}=\Delta\theta/\omega, \quad \omega=l/\mathcal{J} \ . \tag{24}$$

The angular velocity ω is given by the total angular momentum l of the system divided by the total moment of inertia. In this simple relation we shall ignore the fact that the moment of inertia changes continually during the interaction as a result of shape changes and instead assume a simple rigid rotation without axial spin components ($K=0$). These are crude assumptions, but the inherent inaccuracy of the method does not warrant further refinements. Two different estimates of the constant moment of inertia, $\mathcal{J}$, of Eq. (24) have been used in the derivation of the reaction times, namely

$$\mathcal{J}_A=1.4\mathcal{J}_0 \ \text{ or } \ \mathcal{J}_B=0.5[\mathcal{J}_{\mathrm{tot}}(\mathrm{in})+\mathcal{J}_{\mathrm{tot}}(\mathrm{out})] \ , \tag{25}$$

where $\mathcal{J}_0$ is the rigid spherical moment of inertia of the combined system and $\mathcal{J}_{\mathrm{tot}}(\mathrm{in})$ and $\mathcal{J}_{\mathrm{tot}}(\mathrm{out})$ are the total rigid moment of inertia for touching spheres corresponding to the entrance or exit channel mass asymmetry, respectively. Sharp surface spheres with a radius parameter of $r_0=1.16$ fm were assumed in both cases.

In order to relate the relaxation of the mass asymmetry degree of freedom to the reaction time, we have divided the mass distribution corresponding to projectile-like capture products into three bins, each containing one-third of the cross section. The average mass corresponding to each bin, $\langle A\rangle$, was computed and the results are listed in Table VIII along with a normalized measure of the degree of mass drift toward symmetry defined as

$$\frac{\Delta A}{\Delta A_{\max}}=\frac{A_p-\langle A\rangle}{A_p-A_s} \ , \tag{26}$$

where A_s is the symmetric mass

$$A_s=\tfrac{1}{2}(A_p+A_t), \quad \Delta A_{\max}=\tfrac{1}{2}(A_p-A_t) \ , \tag{27}$$

A_p and A_t being the projectile and target masses, respectively.

The mean partial wave associated with each mass bin was estimated on the following basis. The partial wave distribution for capture reactions, and the associated transmission coefficients T_l, were obtained from model calculations as described in Sec. IV D. This distribution was divided into three partially overlapping bins, each encompassing one-third of the capture cross section, with a falloff toward high partial waves given by the T_l's for capture. It is furthermore assumed that the most symmetric mass bin is associated with the angular momentum bin corresponding to the smallest spins, etc. The mean angular momentum, as well as the corresponding angle of rotation $\Delta\theta$ and the reaction times τ_A and τ_B calculated with the two different assumptions on the moment of inertia, are listed in Table VIII.

The correlation between the mean normalized mass drift toward symmetry, $\Delta A/\Delta A_{\max}$, and the reaction time, determined from the angles of rotation, is shown in Fig. 19, for the cases listed in Table VIII. We find a surprising universality in this correlation irrespective of the target species[13] and the bombarding energy.[43,44] It indicates that the drift toward mass symmetry occurs as an overdamped motion given by

$$\Delta A/\Delta A_{\max}=1-\exp[-(t-t_0)/\tau] \ , \tag{28}$$

and that the time constant common to all systems is $\tau=(5.3\pm 1)\times 10^{-21}$ s. There appears to be a time delay of $\tau_0\sim 1\times 10^{-21}$ s before (and after) mass drift sets in. We interpret this as the time from contact until a sizable neck is generated between the interacting ions plus the time of neck constriction prior to scission.

An important result of this analysis is the apparent

TABLE VIII. Mass drift, radial injection energy, angles of rotation, and reaction times for ^{238}U induced reactions. $E_R(l)=E_{\mathrm{c.m.}}-V(l)$, $\langle \Delta A \rangle = A_p - \langle A \rangle$, and $\Delta A_{\max}=\frac{1}{2}(A_p-A_t)$. $\Delta\theta=\pi-\theta_i-\theta_f-\theta$, $\tau_A=\Delta\theta/\langle\omega_A\rangle$, $\omega_A=l/\mathcal{J}_A$, $\mathcal{J}_A=1.4\mathcal{J}_{\mathrm{sph}}$, $\tau_B=\Delta\theta/\langle\omega_B\rangle$, $\langle\omega_B\rangle=l/\mathcal{J}_B$, and $\mathcal{J}_B=\frac{1}{2}[\mathcal{J}_{\mathrm{tot}}(\mathrm{in})+\mathcal{J}_{\mathrm{tot}}(\mathrm{out})]$.

Target	$(E/A)_{\mathrm{lab}}$ (MeV/nucleon)	Bin	$\langle A \rangle$	$\langle l \rangle$ ($\hbar$)	$\frac{\Delta A}{\Delta A_{\max}}$	$\langle E_R \rangle$ (MeV)	$\Delta\theta$ (deg)	τ_A (10^{-21} s)	τ_B (10^{-21} s)
^{27}Al	5.4	1	123	21	~1.0		65	6.9	8.7
		2	143	32	0.90		58	4.1	5.2
		3	166	40	0.68		54	3.1	3.7
	5.9	1	120	27	~1.0	7.5	249	20.9	26.1
		2	143	40	0.91	4.0	239	13.6	17.1
		3	167	48	0.67	0.3	232	10.9	13.2
	6.7	1	117	28	~1.0	23.7	223	18.0	22.4
		2	141	52	0.92	12.0	207	9.0	11.3
		3	167	67	0.68	0.9	195	6.6	8.0
	7.5	1	121	33	~1.0	41.3	211	14.5	18.1
		2	146	61	0.87	25.1	195	7.2	9.1
		3	166	78	0.69	10.2	183	5.3	6.3
^{32}S	5.4	1	154	18	0.90		52	6.7	8.6
		2	167	28	0.75		43	3.6	4.5
		3	185	30	0.48		41	3.0	3.5
	6.7	1	130	27	~1.0	22.0	245	21.2	27.1
		2	151	49	0.83	13.5	232	11.1	14.1
		3	169	64	0.67	4.7	222	8.1	9.9
	7.5	1	130	34	~1.0	42.4	223	15.3	19.6
		2	157	63	0.78	28.0	207	7.7	9.8
		3	174	81	0.63	14.5	196	5.7	6.8
^{35}Cl	5.4	1	151	21	0.87		62	7.0	9.1
		2	179	33	0.75		53	3.9	4.8
		3	200	52	0.55		38	1.8	2.1
	5.9	1	135	28	~1.0	6.3	249	31.2	27.1
		2	162	42	0.75	2.3	239	16.3	17.4
		3	188	69	0.49		232	12.3	9.5
	6.7	1	132	32	~1.0	27.6	204	15.1	19.6
		2	158	58	0.79	16.8	190	7.8	10.0
		3	177	75	0.60	6.2	179	5.7	6.9
	7.5	1	131	37	~1.0	50.4	183	11.7	15.2
		2	158	67	0.79	36.0	168	6.0	7.6
		3	183	87	0.54	21.3	157	4.3	5.2
^{40}Ca	5.4	1	216	11	0.22		53	11.9	13.9
		2	229	18	0.09		41	5.6	6.1
		3	233	23	0.05		30	3.2	3.8
	5.9	1	177	23	0.6	1.0	93	9.9	12.8
		2	208	36	0.30		63	4.3	5.0
		3	227	45	0.1		48	2.6	2.9
	6.7	1	155	28	0.84	25.7	157	13.7	18.1
		2	184	51	0.55	17.7	115	5.5	7.0
		3	205	66	0.33	11.2	73	2.7	3.1
	7.5	1	152	37	0.87	50.7	224	14.8	19.5
		2	180	67	0.59	38.1	170	6.2	7.9
		3	202	87	0.37	25.5	110	3.1	3.6

TABLE VIII. (*Continued*).

Target	$(E/A)_{\mathrm{lab}}$ (MeV/nucleon)	Bin	$\langle A \rangle$	$\langle l \rangle$ ($\hbar$)	$\frac{\Delta A}{\Delta A_{\mathrm{max}}}$	$\langle E_R \rangle$ (MeV)	$\Delta\theta$ (deg)	τ_A (10^{-21} s)	τ_B (10^{-21} s)
^{48}Ca	4.6	1	202	24	0.38		45	4.9	6.2
		2	214	39	0.26		39	2.6	3.1
		3	220	47	0.19		33	1.8	2.1
	4.8	1	193	27	0.47		62	5.9	7.6
		2	209	43	0.31		50	3.0	3.6
		3	217	53	0.22		35	1.7	2.0
	5.0	1	182	31	0.59	3.1	71	5.9	7.8
		2	205	49	0.35	0.8	58	3.1	3.8
		3	218	60	0.21		47	2.0	2.3
	5.4	1	165	37	0.76	11.4	117	8.2	11.0
		2	195	55	0.45	11.2	89	4.2	5.3
		3	214	69	0.26	5.4	72	2.7	3.2
	5.9	1	152	38	0.91	35.4	194	13.1	17.6
		2	185	68	0.58	24.9	170	6.6	8.4
		3	203	88	0.37	14.6	150	4.4	5.2
	6.7	1	148	41	0.94	65.1	202	11.3	15.1
		2	183	83	0.58	49.3	172	6.3	7.0
		3	205	108	0.34	33.3	145	3.5	4.2
	7.5	1	153	55	0.90	94.1	210	9.8	13.2
		2	182	100	0.59	71.0	183	4.7	6.2
		3	203	130	0.37	47.6	149	3.0	3.6
$^{\mathrm{nat}}$Zn	5.4	1	175	16	0.73		57	10.0	13.9
		2	209	31	0.32		44	4.0	5.3
		3	216	40	0.26		38	2.6	3.4
	6.7	1	186	34	0.60	47.5	75	6.2	8.5
		2	213	62	0.28	40.9	69	3.1	4.1
		3	220	80	0.21	34.5	64	2.2	2.8
	7.5	1	184	42	0.63	86.4	91	6.1	8.4
		2	212	77	0.30	76.1	90	3.3	4.4
		3	218	99	0.23	66.4	87	2.5	3.2

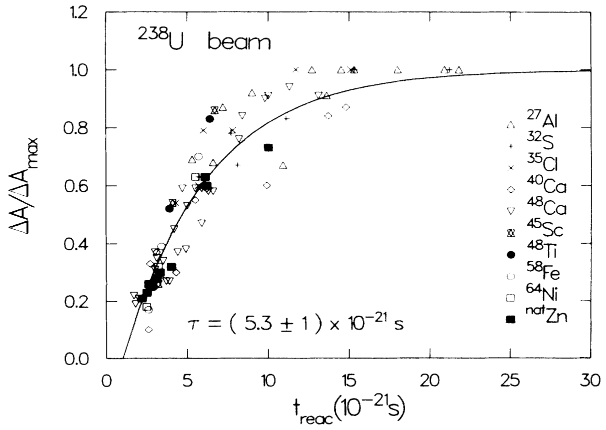

FIG. 19. Normalized mass drift $\Delta A/\Delta A_{\mathrm{max}}$ as a function of the reaction time. The solid curve represents the best fit to the data using Eq. (28). The parameters for the curve are given in the text.

temperature independence of the drift rate in the mass asymmetry degree of freedom. This point is illustrated more clearly in Fig. 20, where the data are divided into three bins according to the estimated energy E^* of the would-be compound system. This represents an upper bound to the excitation energy during mass relaxation, the actual excitation energy being reduced by some 5–20 MeV of deformation energy relative to the (spherical) compound nucleus. The solid curves in this figure are identical, representing the best fit to the entire set of data. The consequences of this apparent temperature independence of the characteristic time for the mass drift mode is discussed in further detail in the following subsection.

The effect of using smoothly overlapping partial l distributions for each of the three mass bins is illustrated in Fig. 21. Data for the seven different bombarding studied for the ^{238}U + ^{48}Ca system are shown. In the derivation of the data points shown in panel (a) of Fig. 21, a sharp cutoff l distribution is assumed for the capture reactions.

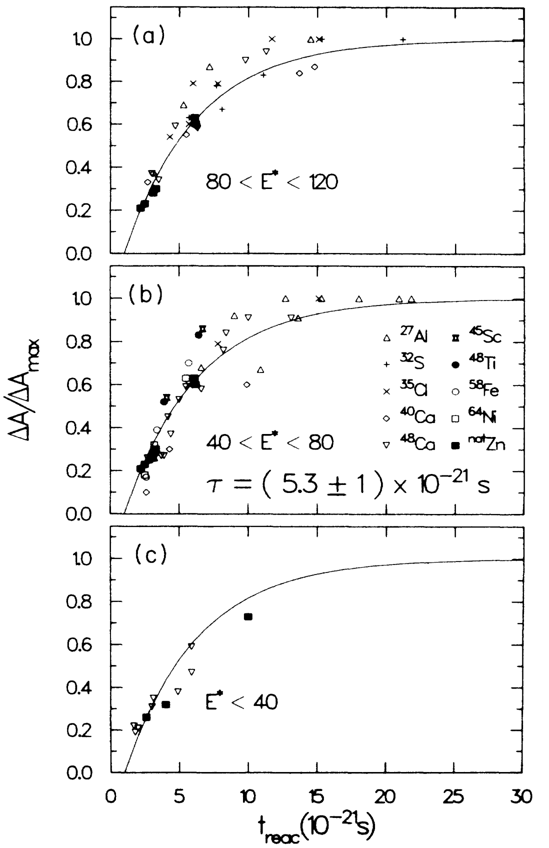

FIG. 20. Illustration of the temperature independence of the time constant for mass drift toward symmetry. The data are divided into three excitation energy bins. Identical curves based on the best fit to the data in Fig. 19 are shown in the three panels for comparison.

This is again divided into three sharply divided bins, each containing one-third of the cross section. The average l value of each bin is used to compute the associated reaction time. As known from numerous other studies, this method results in a severe underestimation of l values contributing to both complete fusion and capture reactions near or below the barrier. In Fig. 21(a) this underestimate results in excessively long reaction times for low bombarding energies. In panel (b) of Fig. 21 we show reaction times which are computed on the basis of smooth l distributions. In this case low- and high-energy points fall on the same curve. This illustrates the importance of using correct l distributions, which agree with subbarrier cross sections, also in this type of analysis.

C. Dissipation mechanism in the mass drift mode

The tendency for mass equilibration observed in the present data is thought to be caused by the fact that the minimum in the potential energy surface for the systems studied in the present work occurs for equal mass divisions. The mass dependence of the potential energy is reasonably well represented by a parabola of the form $U=\frac{1}{2}k(\langle A\rangle - A_s)^2$, where k is practically independent of the temperature. This leads to a driving force for the

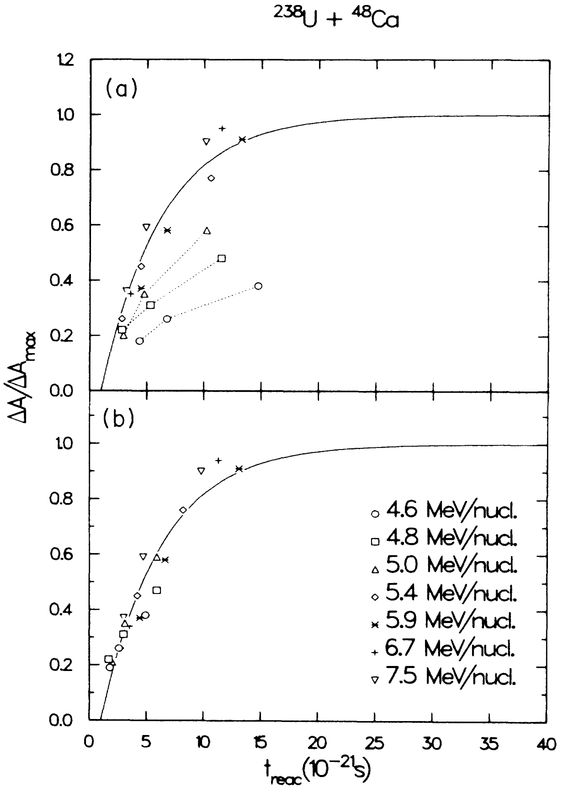

FIG. 21. Illustration of the importance of using smooth angular momentum distributions. The data are for the $^{238}U+^{48}Ca$ system at seven different bombarding energies. The data shown in panel (a) are derived using a sharp boundary between adjacent angular momentum bins, whereas the results assuming smoothly overlapping angular momentum bins are shown in panel (b).

mass drift mode of the form

$$F_c=\frac{dU}{d\langle A\rangle}=-k(\langle A\rangle - A_s) \ . \tag{29}$$

The force constant k may be estimated from the liquid drop model[18] of symmetric and asymmetric saddle shapes to be $k\sim 0.0035$ MeV/u^2 for all the systems studied here. In an *overdamped* motion this driving force will be balanced by the dissipative friction force

$$F_d=\frac{1}{m}\frac{d\langle A\rangle}{dt} \ , \tag{30}$$

where m is the mobility which could depend on temperature. From these equations one obtains

$$\frac{A_p-\langle A\rangle}{A_p-A_s}=\frac{\langle\Delta A\rangle}{\Delta A_{\max}}=1-\exp\left[-\frac{t-t_0}{\tau}\right] \ , \tag{3.1}$$

where

$$\tau=\frac{1}{mk} \ . \tag{32}$$

The temperature independence of the dissipation as observed for motion in the mass asymmetry degree of freedom is characteristic for one body dissipation, which occurs in media[14] where the mean free path of the particles is long or comparable to the dimensions of the object. In the nucleus this form of dissipation is realized by the interaction between single nucleons and the nuclear surface. The relative importance of one-body dissipation, as opposed to two-body dissipation which arises from collisions between nucleons inside the nuclear medium, depends on the mean free path.[45] If the mean free path is much shorter than the nuclear dimensions, many two-body collisions would occur before an interaction with the nuclear surface could take place. In this case one would expect ordinary viscous flow associated with the two-body dissipation mechanism to prevail. If, however, the mean free path is longer than or comparable to the nuclear dimensions, one will expect the one-body particle-surface dissipation mechanisms to dominate. The difference in temperature dependence for the two mechanisms is a clue to the relative importance of one-body versus two-body dissipation in nuclei. As a Fermi liquid, the dissipation properties of nuclear matter may be compared to those of bulk liquid ^{3}He. In this latter case it has been observed that the viscosity is inversely proportional to the square of the temperature, $\eta \sim 1/T^2$, as expected from a two-body dissipation mechanism in the framework of the general Landau theory.[46] The observation that the characteristic time constant τ for the mass asymmetry relaxation is independent of the temperature lends strong support to the assumption that the one-body dissipation is responsible for the dissipation in the nuclear case. In the following we will therefore compare the observed characteristic times with estimates for one-body dissipation for simplified geometries.

The general expression for one-body dissipation for a dinuclear system connected by small neck of cross section a may be written[15]

$$-\frac{dE}{dt}=\rho\bar{v}\oint_1 d\sigma(\dot{n}-D_i)^2+\rho\bar{v}\oint_2 d\sigma(\dot{n}-D_2)^2 + \tfrac{1}{4}\rho\bar{v}(2\dot{z}^2+\dot{x}^2)a+\tfrac{16}{9}\rho\bar{v}\frac{\dot{V}_1^2}{a}\ , \tag{33}$$

where ρ, $\bar{v}$, $\dot{n}$, and D_i are the nuclear mass density, mean particle speed, surface velocity perpendicular to a surface element $d\sigma$, and general translational and rigid rotational drift velocity of each of the two partners. The quantities $\dot{x}$ and $\dot{z}$ describe the relative motion of the two reaction partners, whereas $\dot{V}_1$ denotes the rate of change of the volume of one of the fragments. As can be seen, the expression contains no temperature dependent quantities (both $\bar{v}$ and ρ are practically constant in the temperature range considered here). Presently, we will consider the situation where the relative motion between the two ions has been dissipated both in the radial and tangential directions. We may therefore disregard the third term in Eq. 33, which represents the dissipation in the relative motion. If we furthermore assume that the system is represented by two spheres with a common window of area $a=\pi r_w^2$, Eq. (33) reduces to

$$-\frac{dE}{dt}=4\pi\rho\bar{v}(R_1^2\dot{R}_1^2+R_2^2\dot{R}_2^2)+\tfrac{16}{9}\rho\bar{v}\frac{\dot{V}_1^2}{a}\ , \tag{34}$$

where R_i, $i=1,2$, are the radii of fragment 1 or 2, respectively. Here the first two terms arise from the wall dissipation generated by the expansion of one fragment and the corresponding contraction of the other. The third term represents the dinuclear dissipation associated with the mass flow through the interconnecting neck. It should be noted, however, that this term is derived under the assumption that the window radius is much smaller than the nuclear dimensions, an assumption which may not be fulfilled for the quasifission reactions.

Using the relation $R_i=r_0A_i^{1/3}$ and

$$\rho\bar{v}r_0^4=\frac{27}{32\pi}\left[\frac{\pi}{3}\right]^{1/3}\hbar\ ,$$

we find

$$-\frac{dE}{dt}=\frac{3}{8}\left[\frac{\pi}{3}\right]^{1/3}\hbar\left[\frac{1}{A_1^{2/3}}+\frac{1}{A_2^{2/3}}+\frac{64}{9}\left[\frac{r_0}{r_w}\right]^2\right](\Delta\dot{A})^2,$$

$$-\frac{dE}{dt}=\frac{3}{8}\left[\frac{\pi}{3}\right]^{1/3}\frac{h}{A^{2/3}}\left[\left[\frac{A}{A_1}\right]^{2/3}+\left[\frac{A}{A_2}\right]^{2/3}+\frac{64}{9}\left[\frac{R}{r_w}\right]^2\right](\Delta\dot{A})^2 \tag{35}$$

$$=2.5\times10^{-22}A^{-2/3}\left[\left[\frac{A}{A_1}\right]^{2/3}+\left[\frac{A}{A_2}\right]^{2/3}+\frac{64}{9}\left[\frac{R}{r_w}\right]^2\right](\Delta\dot{A})^2\ (\text{MeV/s})\ , \tag{36}$$

where A is the mass number and R the spherical radius of the compound system and $\Delta A=A_s-A_1=A_2-A_s$. We find that the third term associated with mass transfer through the interface is substantially larger than the first terms, which are appropriate for mononuclear systems. For a typical system, say ^{48}Ca+^{238}U with a interconnecting window of radius $r_w=0.3R$, we find

$$\begin{aligned}-\frac{dE}{dt}&=(1/m)(\Delta\dot{A})^2\\&=2.5\times10^{-22}A^{-2/3}(3.3+1.1+79)(\Delta\dot{A})^2\ (\text{MeV/s})\\&=4.8\times10^{-22}(\Delta\dot{A})^2\ (\text{MeV/s})\ .\end{aligned} \tag{37}$$

This results in a characteristic relaxation time for the mass asymmetry mode of $\tau=1/mk=1.4\times10^{-19}$ s, which is about 26 times longer than observed experimentally.

One may expect that most of the mass transfer observed in quasifission reactions takes place while the interconnecting window is too large to justify the dinuclear description of the dissipation. We therefore compare the measured relaxation time with that expected for mononuclear wall dissipation only, i.e., disregarding the last term in Eq. (35). In this case we find

$$-\frac{dE}{dt}=2.5\times10^{-22}A^{-2/3}[(A/A_1)^{2/3}+(A/A_2)^{2/3}](\Delta\dot{A})^2 , \tag{38}$$

or, for symmetric systems,

$$-\frac{dE}{dt}=7.95\times10^{-22}A^{-2/3}(\Delta\dot{A})^2 . \tag{39}$$

The resulting characteristic mass relaxation times for the ^{48}Ca+^{238}U system ranges from $\tau=4.6\times10^{-21}$ s for mass symmetry to $\tau=6.4\times10^{-21}$ s for the entrance channel mass asymmetry, which is in remarkable agreement with the experimental value of $\tau_{\text{expt}}=(5.3\pm1)\times10^{-21}$ s.

Also, the independence of the observed relaxation times for mass relaxation of all the systems considered is in agreement with the wall dissipation picture since the mobility m is expected to change, due to the $A^{2/3}$ factor, by less than 10% over the range of systems studied in the present work. As already mentioned, the force constant k, which in conjunction with the mobility m determines the mass asymmetry relaxation times, is also expected to remain virtually constant over this range of masses.

In conclusion, we find that the mononuclear wall formula provides a remarkably good description of the observed relaxation times for the mass asymmetry mode. The role of additional dissipation arising from the use of the dinuclear dissipation expression remains, however, open to question. The exact conditions for the validity of the mononuclear as opposed to the dinuclear description, and the different physical contents of these alternate descriptions, need to be more clearly understood.

VI. TOTAL KINETIC ENERGIES

The average total kinetic energies for symmetric mass divisions obtained in the present experiment are listed in Table II and plotted in Fig. 22 as solid squares as a function of the parameter $Z^2/A^{1/3}$. Similar data taken from the literature are shown as open triangles,[17] open squares,[47] and solid circles,[13] respectively. The solid line represents a best linear fit to the previously available data obtained by Viola *et al.*, see Ref. 17. We note that this straight line fit gives a good representation of all of the available data, including the heaviest system, namely ^{238}U+$^{\text{nat}}$Zn, obtained in the present experiment. The present data, and those of Ref. 13, which both contain quasifission products to varying degrees, do not show any deviation from the systematics from systems with purely compound nucleus fission, generally at lower values of $Z^2/A^{1/3}$. In the case of a creeping motion toward scission, this result is consistent with scission shapes that are essentially identical for all systems and for the two types of reactions. The dashed curve in Fig. 22 represents the results of a recent dynamical calculation of Nix and Sierk,[48] which is based on a modified surface and window dissipation mechanism. Although this calculation gives an accurate description of the total kinetic energy release for a wide range of systems, it underpredicts this quantity for the heaviest systems, where quasifission processes dominate. This discrepancy may possibly arise because the quasifission process follows trajectories in configuration space different from those of the fission process, where the system proceeds on a path all the way from the saddle point to the scission point. The calculation applies only to this latter type of trajectories and may not be representative of a quasifission process. It is, however, also possible that it is caused by inadequacies in the assumed dissipation mechanism. The total kinetic energy is quite sensitive both to the assumed transition from wall to window dissipation[49] and the possible premature rupture of the connecting neck.[50]

In Fig. 23 we show the average total kinetic energy for symmetric mass division as a function of the available excitation at the scission point, given by $E^+=E^*-Q_0-E_K$, where E^* is the excitation energy of the compound system, Q_0 is the Q value for symmetric mass division, and E_K is the average kinetic energy. It is found that within the experimental uncertainty of the data the average kinetic energy is independent of the excitation energy. This result indicates that the additional kinetic energy is completely damped away, i.e., converted to intrinsic excitations of the system. Also, this aspect of the quasifission process agrees with that of the normal fission decay of hot nuclei, where only a very weak dependence of the final to-

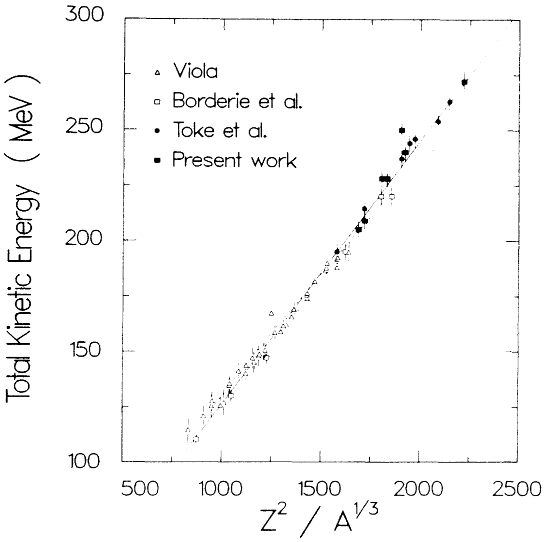

FIG. 22. Average total kinetic energies for symmetric mass divisions are shown as a function of the parameter Z^2/A. Data points taken from Refs. 17, 47, 13, and the present work are shown as open triangles, open squares, solid points, and solid squares, respectively. The solid line represents the empirical systematics of Viola *et al.* (Ref. 17), whereas the dashed curve is taken from Ref. 48.

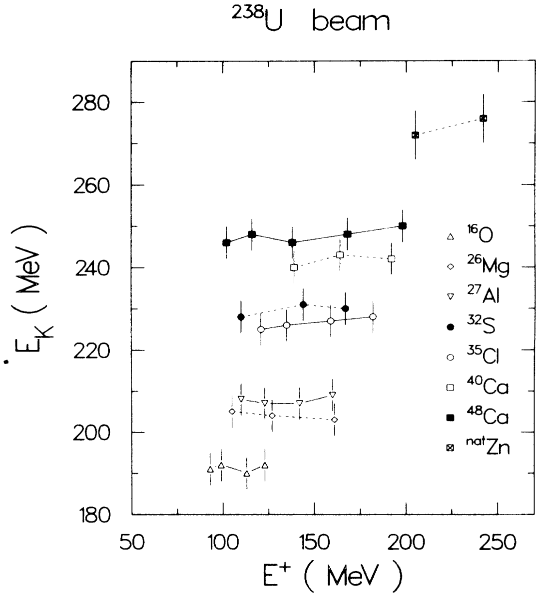

FIG. 23. The average kinetic energy for symmetric mass division is shown as a function of the excitation energy at the scission point, E^+, for the targets indicated in the figure.

tal kinetic energy on the excitation energy and angular momentum of the system has been observed.[51]

In Fig. 24 the full widths at half maximum of the total kinetic energy distribution for symmetric mass divisions are shown as a function of the available excitation energy at the scission point, $E^+=E^*-Q_0-E_K$ [panel (a)] and the compound system E^* [panel (b)]. In general, the total kinetic energy distribution broadens with excitation energy, as expected. We find, however, that the width is somewhat better correlated with the excitation energy at the scission point, E^+, than with the compound system excitation energy E^*. This observation is consistent with the notion that the descent toward the scission point is subject to considerable energy dissipation, with little or no relative kinetic energy in the relative motion of the two nascent fragments being present at this point.

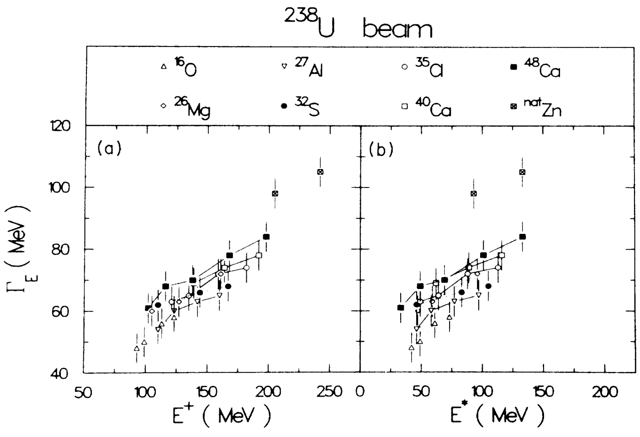

FIG. 24. The width (FWHM) of the total kinetic energy distribution for symmetric mass divisions is shown as a function of excitation energy at scission, E^+, panel (a), as well as the compound system, E^*, panel (b), for the targets indicated in the figure.

The total reaction times, obtained from the measured rotation angles (see Sec. V B) do, however, impose a limit on the magnitude of the dissipation forces. From the observed quantities, reaction times, mass drift rates, and kinetic energy damping, it is, in principle, feasible to set both lower and upper limits for the dissipative forces. These must be sufficiently weak to allow the rather short reaction times observed, but also strong enough to damp out the kinetic energy, which is remarkably independent of the initial kinetic energy, as illustrated in Fig. 23. Due to the complexity of the dynamics of quasifission processes, it is, however, not feasible to determine these limits from the observed quantities in a simple model independent way. One must rely on detailed model calculations[52] based on specific dissipation mechanisms, as well as a number of other assumptions, and compare to the experimental results. We feel that such an analysis lies outside the scope of the present work and it has therefore not been pursued.

Instead, we consider the striking constancy of the total kinetic energy release for symmetric fragmentation as displayed in Fig. 23. If the dissipation is sufficiently strong to give rise to a creeping motion toward scission over the entire excitation energy range of the present data, this is perhaps not surprising, since the total kinetic in this case is just the Coulomb repulsion between the fragments at scission and the correlation illustrated in Fig. 22 speaks strongly for constant scission shapes. If, however, the descent toward scission is only partially damped, the constancy of the total kinetic energy implies also a constant, i.e., a temperature independent dissipation mechanism.

The division between translational and excitation energy of the potential energy difference between the saddle and scission points has been a long-standing question in fission research, which has been difficult to settle due to the lack of convincing experimental evidence. Experimental, but still somewhat model dependent, information on the prescission kinetic energy for low energy fission has recently been obtained from an analysis of the observed increase of symmetric fission yield with increased excitation energy in neutron induced fission.[53] In the region of Z and A values studied, it was found that the prescission kinetic energy increases with fissility of the system according to the formula

$$E_K^{\rm pre}=0.0158Z^2/A^{1/3}-11.3\ \text{MeV}\ ,$$

or, e.g., $E_K^{\rm pre}=18.8$ MeV for the system ^{238}U$+^{48}$Ca. This indicates that the descent toward scission is only partially damped with about 35–40 % of the 60 MeV potential energy difference between the saddle and scission points converted into translational energy, whereas the remaining 60–65 % is converted into internal excitations. This is in good agreement with the prediction of $E_K^{\rm pre}=21$ MeV obtained in an earlier work by Sierk and Nix[54] on the basis of the unmodified one-body dissipation mechanism (wall and window). It also agrees with model calculations by Swiatecki,[33] and it is perfectly compatible with the delay, $\simeq(1-2)\times10^{-21}$s, seen in the mass relaxation curves in Figs. 19 and 20.

The constancy of the total kinetic energy with excitation energy again supports the notion that nuclear dissipation is basically of a one-body type, in agreement with the observed temperature independence of the energy dissipation. Since the motion toward scission appears to be only partially damped, one would be sensitive to a possible temperature dependence, as, e.g., the $1/E^*$ dependence expected for bulk viscosity. Such a decrease of the dissipation, which presumably would lead to an increase of the order of 10–20 MeV total kinetic energy with temperature, is not seen, cf. Fig. 23. The weak increase indicated by the measurements can be fully understood as an (attenuated[51]) angular momentum effect. This observation strengthens the conclusion obtained from the analysis of the mass asymmetry relaxation rates, namely that the prevailing part of the nuclear dissipation mechanism, whether mononuclear or dinuclear, is of one-body character at these temperatures.

VII. SUMMARY

We have studied the different aspects of quasifission processes in interactions between a beam of ^{238}U and targets ranging from ^{16}O to $^{\mathrm{nat}}$Zn at relative kinetic energies between 4.6 and 7.5 MeV/nucleon. It is found that the quasifission processes account for an important part of the total reaction cross section providing a natural link between the more peripheral deeply inelastic scattering processes and the complete fusion, which occurs for more central collisions. The quasifission reaction constitutes the mass drift mode of heavy ion interactions and is therefore only discernible for interactions between projectiles and targets of distinctly different mass. In heavy systems—the only region where quasifission processes have been observed—the underlying potential favors mass drift toward symmetry in accordance with the observed direction of the mass flow. Varying degrees of mass relaxation are observed for different targets and bombarding energies. For the lighter targets, e.g., ^{16}O, ^{24}Mg, and ^{27}Al, the quasifission process resembles mostly the fission decay after compound nucleus formation. In this region the mass drift toward symmetry is almost complete and only small variations in the mass distributions as a function of scattering angle together with an enhanced angular anisotropy reveal the quasifission origin of the products. For somewhat heavier targets the mass drift toward symmetry is clearly incomplete and the quasifission products are easily identifiable, while for the very heaviest targets the quasifission products overlap with the products of deeply inelastic scattering reactions, and there is no clear distinction between the two processes.

The measured cross sections for capture reactions, which include quasifission and complete fusion-fission processes, and for complete fusion reactions, are analyzed within the framework of the extra- and extra-extra-push model. The capture and complete fusion processes are associated with reaction trajectories which pass inside the conditional and the true saddle points, respectively, in this model. It is found that the data are in qualitative agreement with the scaling properties of the model. Universal scaling can be determined from the observed set of cross sections provided that a fast charge equilibrium in the entrance channel is assumed. This latter modification removes a previous inconsistency between the thresholds for capture and complete fusion. While the qualitative features of the theoretical model are strikingly reflected in the experimental systematics, there remains a significant discrepancy between experimental and theoretically calculated threshold and slope parameters.

The partial relaxation of the mass asymmetry and the finite angle of rotation in quasifission reactions makes it possible to see a correlation between the fragment mass and the scattering angle. This correlation allows for the determination of reaction times (using plausible assumptions about the contributing l values and the moment of inertia of the system during the process). It has been found that the mass drift toward symmetry occurs on a time scale of $t=(2-10)\times10^{-21}$ s following an exponential curve, which is characteristic of a strongly damped motion. An important result of this study is the universality of the time constant in the drift toward symmetry. We found that all of the present data are consistent with a time constant of $\tau=(5.3\pm1.0)\times10^{-21}$ s, irrespective of target mass and bombarding energy. The latter observation strongly supports the picture that the nuclear dissipation is basically of one-body type, i.e., the energy loss is caused by interactions of the constituent particles with the nuclear surface. The alternative dissipation mechanism, namely the two-body dissipation giving rise to bulk viscosity, is expected to be inversely proportional to the excitation energy. This would have given rise to a difference in time constants of a factor of 2–3 over the range of bombarding energies of the present experiment. Such a dependence is inconsistent with the data, thus lending strong support to the assumption of one-body nuclear dissipation. The measured relaxation time is in quantitative agreement with model estimates assuming the mass asymmetry motion to be of the mononuclear type.

The total kinetic energies for symmetric fragmentation have been studied and found to follow the empirical systematics obtained previously from compound fission reactions. The total kinetic energy extrapolates linearly and proportionally in the quantity Z^2/A to be heaviest systems, whereas a recent calculation based on a one-body dissipation mechanism of reduced strength tends to underestimate the total kinetic energy for the heaviest systems. It is furthermore observed that the total kinetic energy is independent, within the experimental accuracy, of the beam energy and consequently the excitation energy of the system. In view of the recent tentative result that the motion toward scission is only partially damped, this result means that this damping is independent of temperature over a larger range, again supporting the assumption that the nuclear dissipation is dominated by one-body collisions between independent nucleons and the nuclear surface. Several aspects of the present study thus confirm this picture. The present study is sensitive to the exact strength of the dissipation function only in a model dependent way. In particular, it is emphasized that the transition from the mononuclear to the dinuclear regime needs further theoretical clarification.

ACKNOWLEDGMENTS

The authors have benefited from several illuminating discussions with R. Donangelo, H. Feldmeier, and W. J. Swiatecki, as well as several other colleagues, whose advice is greatly appreciated. We wish to thank the staff of the Unilac accelerator for their tireless effort in delivering a high quality uranium beam for the experiment. The effort of H. Folger and his co-workers in preparing several very difficult targets is acknowledged. The assistance of G. Augustinski, H. J. Beeskow, H. Daues, W. Quick, and M. Ludwig is appreciated. This work was supported by the Danish Natural Science Foundation and the U. S. Department of Energy under Contract No. W-31-109-ENG-38.

---

[*] On leave from Institute of Modern Physics, Lanzhou, People's Republic of China.

[†] On leave from University of Cracow, Cracow, Poland.

[‡] Now at McGill University, Montreal, Canada.

[§] Now at University of Rochester, Rochester, NY 14627.

[**] On leave from Argonne National Laboratory, Argonne, IL 60439.

[††] Now at University of Tennessee, Knoxville, TN 37921.

[1] B. Heusch, C. Volant, H. Freiesleben, R. P. Chestnut, K. D. Hildenbrand, F. Pühlhofer, W. F. W. Schneider, B. Kohlmeyer, and W. Pfeffer, Z. Phys. A **288**, 391 (1978).

[2] C. Lebrun, F. Hanappe, J. F. Lecolley, F. Lefebvres, C. Ngô, J. Péter, and B. Tamain, Nucl. Phys. A **321**, 207 (1979).

[3] B. Borderie, M. Berlanger, D. Gardes, F. Hanappe, L. Nowicki, J. Péter, B. Tamain, S. Agarwall, J. Girard, C. Grégoire, J. Mutuszek, and C. Ngô, Z. Phys. A **299**, 263 (1981).

[4] C. Grégoire, C. Ngô, and R. Remaud, Phys. Lett. **99B**, 17 (1981).

[5] B. B. Back, H.-G. Clerc, R. R. Betts, B. G. Glagola, and B. D. Wilkins, Phys. Rev. Lett. **46**, 1068 (1981).

[6] B. B. Back, R. R. Betts, K. Cassidy, B. G. Glagola, J. E. Gindler, L. E. Glendenin, and B. D. Wilkins, Phys. Rev. Lett. **50**, 818 (1983).

[7] M. B. Tsang, D. Ardouin, C. K. Gelbke, W. G. Lynch, Z. R. Xu, B. B. Back, R. R. Betts, S. Saini, P. A. Baisden, and M. A. McMahan, Phys. Rev. C **28**, 747 (1983).

[8] M. B. Tsang, H. Utsomomiya, C. K. Gelbke, W. G. Lynch, B. B. Back, S. Saini, P. A. Baisden, and M. A. McMahan, Phys. Lett. **129B**, 18 (1983).

[9] B. B. Back, Phys. Rev. C **31**, 2104 (1985); **32**, 1786 (1985).

[10] B. B. Back, R. R. Betts, J. E. Gindler, B. D. Wilkins, S. Saini, M. B. Tsang, C. K. Gelbke, W. G. Lynch, M. A. McMahan, and P. A. Baisden, Phys. Rev. C **32**, 195 (1985); **33**, 385 (1986).

[11] R. Bock, Y. T. Chu, M. Dakowski, A. Gobbi, E. Grosse, A. Olmi, H. Sann, D. Schwalm, U. Lynen, W. F. J. Müller, S. Bjørnholm, H. Esbensen, W. Wölfli, and E. Morenzoni, Nucl. Phys. A **388**, 334 (1982); H. Sann, R. Bock, Y. T. Chu, A. Gobbi, A. Olmi, U. Lynen, W. F. Müller, S. Bjørnholm, and H. Esbensen, Phys. Rev. Lett. **47**, 1248 (1981).

[12] G. Guarino, A. Gobbi, K. D. Hildenbrand, W. F. J. Müller, A. Olmi, H. Sann, S. Bjørnholm, and G. Rudolf, Nucl. Phys. **A424**, 157 (1984).

[13] J. Tõke, R. Bock, G. X. Dai, S. Gralla, A. Gobbi, K. D. Hildenbrand, J. Kuzminski, W. F. J. Müller, A. Olmi, H. Stelzer, B. B. Back, and S. Bjørnholm, Nucl. Phys. **A440**, 327 (1985); J. Tõke, R. Bock, G. X. Dai, A. Gobbi, S. Gralla, K. D. Hildenbrand, J. Kuzminski, W. F. J. Müller, A. Olmi, W. Reisdorf, S. Bjørnholm, and B. B. Back, Phys. Lett. **142B**, 258 (1984).

[14] J. Błocki, Y. Boneh, J. R. Nix, J. Randrup, M. Robel, A. J. Sierk, and W. J. Swiatecki, Ann. Phys. (N.Y.) **113**, 330 (1978).

[15] J. Randrup and W. J. Swiatecki, Nucl. Phys. **A429**, 105 (1984).

[16] U. Lynen, H. Stelzer, A. Gobbi, H. Sann, and A. Olmi, Nucl. Instrum. Methods (special issue) **162**, 657 (1979); H. Stelzer, Nucl. Phys. **A354**, 433 (1981).

[17] V. E. Viola, Jr., Nucl. Data Sect. A **1**, 391 (1966); Phys. Rev. C **31**, 1550 (1985).

[18] P. Möller and J. R. Nix, Nucl. Phys. **A281**, 354 (1977).

[19] P. Bond, Phys. Rev. Lett. **52**, 414 (1984); Phys. Rev. C **32**, 421 (1985); **32**, 483 (1985).

[20] H. H. Rossner, J. R. Huizenga, and W. U. Schröder, Phys. Rev. Lett. **53**, 38 (1984).

[21] S. Cohen, F. Plasil, and W. J. Swiatecki, Ann. Phys. (N.Y.) **82**, 557 (1974).

[22] W. Q. Shen and R. Donangelo, unpublished results.

[23] L. C. Vaz and J. M. Alexander, Phys. Rep. **18c**, 2152 (1978); L. C. Vaz, J. M. Alexander, and G. R. Satchler, *ibid.* **69**, 373 (1981).

[24] J. R. Birkelund, L. E. Tubbs, J. R. Huizenga, J. N. De, and D. Sperber, Phys. Rep. **56c**, 107 (1979).

[25] J. Błocki, J. Randrup, W. J. Swiatecki, and C. F. Tsang, Ann. Phys. (N.Y.) **105**, 427 (1977).

[26] W. D. Myers and W. J. Swiatecki, Ark. Fys. **36**, 343 (1967).

[27] P. Möller and J. R. Nix, Nucl. Data Tables **26**, 165 (1981).

[28] C. Y. Wong, Phys. Lett. **31**, 766 (1973).

[29] R. G. Stokstad, Y. Eisen, S. Kaplanis, D. Pelte, V. Smilanski, and I. Tserruya, Phys. Rev. Lett. **41**, 465 (1978).

[30] B. B. Back, R. R. Betts, W. Henning, K. L. Wolf, A. C. Mignerey, and J. M. Lebowitz, Phys. Rev. Lett. **45**, 1230 (1980).

[31] W. Reisdorf, F. P. Hessberger, K. D. Hildenbrand, S. Hofman, G. Münzenberg, K.-H. Schmidt, J. H. R. Schneider, W. F. W. Schneider, S. Sümmerer, G. Wirth, J. V. Kratz, and K. Shlitt, Phys. Rev. Lett. **49**, 1811 (1982).

[32] H. Esbensen, Nucl. Phys. **A352**, 147 (1981).

[33] W. J. Swiatecki, Phys. Scr. **24**, 113 (1981); Nucl. Phys. **A376**, 275 (1982).

[34] S. Bjørnholm and W. J. Swiatecki, Nucl. Phys. **A391**, 471 (1982).

[35] C.-C. Sahm, H.-G. Clerc, K.-H. Schmidt, W. Reisdorf, P. Armbruster, F. P. Hessberger, J. G. Keller, G. Münzenberg, and D. Vermeulen, Z. Phys. **319**, 113 (1984).

[36] K. Lesko, W. Henning, K. E. Rehm, G. Rosner, J. P. Schiffer, G. S. F. Stephans, and B. Zeidman, Phys. Rev. C **34**, 2155 (1986).

[37] D. Schüll, W. C. Shen, H. Freiesleben, R. Bock, F. Busch, D. Bangert, W. Pfeffer, and F. Pühlhofer, Phys. Lett. **102B**, 116 (1981).

[38] R. Donangelo and L. F. Canto, Nucl. Phys. **A451**, 349 (1986).

[39] C.-C. Sahm, H.-G. Clerc, K.-H. Schmidt, W. Reisdorf, P. Armbruster, F. P. Hessberger, J. G. Keller, G. Münzenberg, and D. Vermeulen, Nucl. Phys. **A441**, 316 (1985).

[40]B. B. Back, in *Proceedings of the International School-Seminar on Heavy Ion Physics* (Joint Institute for Nuclear Research, Dubna, 1986).

[41]J. P. Błocki, H. Feldmeier, and W. J. Swiatecki, Gesellschaft für Schwerionenforschung (Darmstadt) Report No. GSI-86-16, 1986.

[42]G. Wolschin and W. Nörenberg, Z. Phys. A **284**, 209 (1978).

[43]W. Q. Shen, J. Albinski, R. Bock, A. Gobbi, S. Gralla, K. D. Hildenbrand, N. Herrmann, J. Kuzminski, W. F. J. Müller, H. Stelzer, and J. Tōke, Europhys. Lett. **1**, (1986).

[44]S. Bjørnholm, *Proceedings of the International Conference on Nuclear Physics on the Occasion of the Golden Jubilee of the Indian Science Academy, Bombay, 1984* (World-Scientific, Singapore, 1985).

[45]W. J. Swiatecki, Lawrence Berkeley Laboratory Report No. LBL-19222, 1985; in *Proceedings of the Niels Bohr Centennial Symposium on Semi-Classical Descriptions of Atomic and Nuclear Collisions*, Copenhagen, 1985, edited by J. de Boer and J. Bang (Elsevier, Amsterdam, 1985).

[46]A. A. Abrikosov and I. M. Khalatnikov, Rep. Prog. Phys. **22**, 329 (1959).

[47]B. Borderie, F. Hanappe, C. Ngô, J. Péter, and B. Tamain, Nucl. Phys. **A220**, 93 (1974).

[48]J. R. Nix and A. J. Sierk, in *Proceedings of the International Conference on Nuclear Physics,* Bombay, 1984 (World-Scientific, Singapore, 1985), p. 365.

[49]A. J. Sierk and J. R. Nix, Phys. Rev. C **21**, 982 (1980).

[50]K. T. R. Davies, R. A. Managan, J. R. Nix, and A. J. Sierk, Phys. Rev. C **16**, 1890 (1977).

[51]B. G. Glagola, B. B. Back, and R. R. Betts, Phys. Rev. C **29**, 486 (1984).

[52]H. T. Feldmeier, Argonne National Laboratory Report ANL-PHY-85-2, 1985; Gesellschaft für Schwerionenforschung (Darmstadt) Report GSI-85-44, 1985.

[53]B. D. Wilkins and J. E. Gindler, in *Proceedings of the International Symposium on Nuclear Fission and Heavy-Ion-Induced Reactions, Rochester, 1986,* edited by W. Schröder (Harwood, New York, 1987).

[54]A. J. Sierk and J. R. Nix, Phys. Rev. C **21**, 982 (1980).

[55]R. Freifelder, P. Braun-Münzinger, P. DeYoung, R. Schicker, S. Sen, and J. Stachel, Phys. Rev. C (to be published).